JGR Solid Earth

RESEARCH ARTICLE
10.1029/2019JB018347

Remote Detection and Location of Explosive Volcanism in Alaska With the EarthScope Transportable Array

Richard W. Sanderson[1], Robin S. Matoza[1], David Fee[2], Matthew M. Haney[3], and John J. Lyons[3]

[1]Department of Earth Science and Earth Research Institute, University of California, Santa Barbara, CA, USA, [2]Wilson Alaska Technical Center, Alaska Volcano Observatory, Geophysical Institute, University of Alaska Fairbanks, Fairbanks, AK, USA, [3]U.S. Geological Survey Volcano Science Center, Alaska Volcano Observatory, Anchorage, AK, USA

Key Points:
- Explosive eruptions from Bogoslof and Cleveland volcanoes are observed on the EarthScope Transportable Array, to more than 2,000 km
- Reverse time migration (RTM) backprojection approach detects and locates infrasound from volcanic and nonvolcanic events
- Advantages and disadvantages are found for multiple RTM algorithms, each with variable detection rates and location accuracy

Supporting Information:
- Supporting Information S1
- Table S1
- Table S2
- Movie S1
- Movie S2
- Movie S3

Correspondence to:
R. W. Sanderson,
rws@ucsb.edu

Citation:
Sanderson, R. W., Matoza, R. S., Fee, D., Haney, M. M., & Lyons, J. J. (2020). Remote detection and location of explosive volcanism in Alaska with the EarthScope Transportable Array. *Journal of Geophysical Research: Solid Earth*, *125*, e2019JB018347. https://doi.org/10.1029/2019JB018347

Received 9 JUL 2019
Accepted 17 JAN 2020
Accepted article online 23 JAN 2020

Abstract The current deployment of the EarthScope Transportable Array (TA) in Alaska affords an unprecedented opportunity to study explosive volcanic eruptions using a relatively dense regional seismoacoustic network. Infrasound monitoring has demonstrated utility for the remote (>250 km range) detection and characterization of volcanic explosions, but previous studies have used relatively sparse regional or global networks. Seventy explosive events from the locally unmonitored Bogoslof volcano (2016–2017) provide a unique validation data set to examine the ability of the TA and other regional networks to detect and locate remote explosive volcanic eruptions in Alaska. With a simple envelope-based reverse time migration (RTM) technique, we are able to detect and locate more than 72% of the 61 Bogoslof infrasound events detected by the Alaska Volcano Observatory. Notably, RTM using only sparse regional infrasound arrays produces results similar to when incorporating the extensive single-sensor TA network, likely due to favorable signal-to-noise ratios, seasonal propagation conditions, and source-receiver geometries. Our implementation also detects and locates explosive eruptions from Cleveland volcano, Alaska, and Bezymianny volcano, Kamchatka, as well as infrasound from nonvolcanic events such as earthquakes. We characterize the success of the RTM algorithm and associated parameter choices using receiver operating characteristic curves, event detection rates, and location accuracy. Our methods are useful for explosive volcanic and nonvolcanic event detection and localization using real-time data and for scanning continuous waveform data archives.

1. Introduction

1.1. Motivation and Background

The deployment of the EarthScope Transportable Array (TA) in Alaska has brought one of the densest ever seismoacoustic networks to one of the world's most active volcanic regions (Figure 1a). Alaska is home to 130 potentially active volcanoes, of which more than 50 have been active in historical times (Cameron et al., 2018). On average, two volcanoes are in a state of eruption every year (Figure 1b) and are capable of sudden, explosive, ash cloud-forming eruptions, which are potentially hazardous to passenger and freight aircraft along this heavily traveled air corridor (Webley & Mastin, 2009). Monitoring of these volcanoes is performed at the Alaska Volcano Observatory (AVO) by integrating multiple ground-based and satellite monitoring technologies (e.g., Coombs et al., 2018). However, Aleutian volcanoes in particular represent a formidable monitoring challenge. Because of their remote locations, many volcanoes are not instrumented, which is also the case for the majority of potentially active volcanoes worldwide (National Academies of Sciences, Engineering, & Medicine, 2017). Eruptions of Okmok and Kasatochi in 2008 exemplify these challenges, as each volcano produced large atmospheric ash releases with little warning. Despite local instrumentation, precursory indicators at Okmok were few (Haney, 2010). In contrast, precursors at Kasatochi were more numerous but limited to seismic observation from more than 40 km away (Waythomas et al., 2010).

Volcanic eruptions produce seismic, acoustic, and air-ground coupled wavefields, each of which help provide constraints on internal and external volcanic processes (Chouet & Matoza, 2013; Fee & Matoza, 2013; Johnson & Ripepe, 2011; Matoza et al., 2019). Infrasound (acoustic waves <20 Hz) is well suited to remote detection (De Angelis et al., 2012; Fee et al., 2013; Garcés et al., 2008; Matoza et al., 2007; Matoza, Le Pichon, et al., 2011; Matoza, Vergoz, et al., 2011; Matoza et al., 2013; Ripepe et al., 2018). Infrasound attenuation is low, and infrasound can often be recorded thousands of kilometers from the source (Drob et al., 2003;

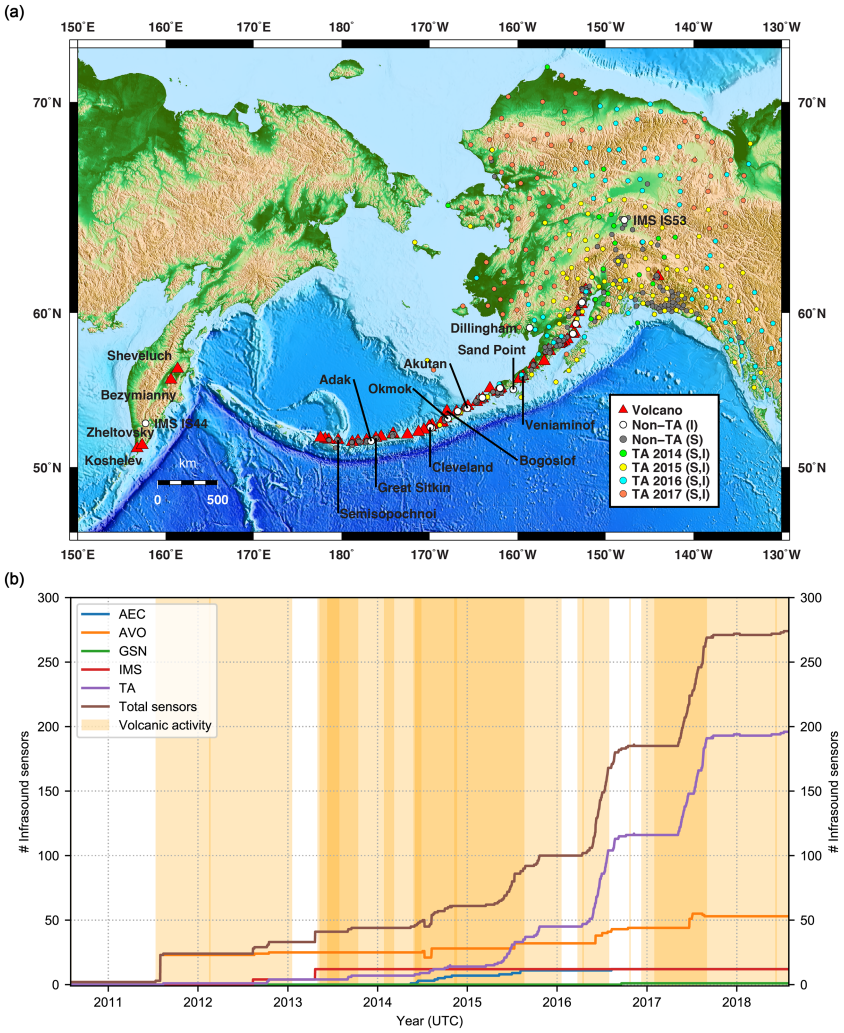

Figure 1. (a) Locations of historically active volcanoes and available seismic (S) and infrasound (I) data in Alaska. Volcanoes and infrasound arrays that are referenced in this study are labeled. (b) Evolution of the number of infrasound sensors deployed within 3,000 km of Bogoslof, 2011–2018. The TA has greatly increased the infrasound recording capacity in Alaska, with TA capacity outnumbering all other networks combined. Overlapping eruptive episodes from multiple volcanoes are shown as orange bars (Alaska Volcano Observatory, 2019).

Le Pichon et al., 2009; Waxler, 2017). Further, infrasound data reduces ambiguity in explosive eruption detection compared to seismic data alone and thus also provides value in the quantification and modeling of subaerial eruptive processes (Harris & Ripepe, 2007; Johnson & Aster, 2005; Marchetti et al., 2004; Marchetti et al., 2013; Matoza et al., 2007; Ripepe et al., 2007; Vergniolle & Caplan-Auerbach, 2006). In cloudy weather conditions, satellite observations of hot material and plumes are limited, where infrasound is unaffected (Fee, Steffke, & Garcés, 2010; Garcés et al., 2008; Matoza, Le Pichon, et al., 2011; Pyle et al., 2013). Lighting detection can also serve as a useful proxy for atmospheric injection, but not all ash-producing eruptions produce lightning (Behnke & McNutt, 2014; Haney, Van Eaton, et al., 2020; McNutt & Williams, 2010; Van Eaton et al., 2016).

Global infrasound networks have been shown to be effective at detecting relatively violent eruptions, even in remote locations (Dabrowa et al., 2011; Evers & Haak, 2005; Fee, Steffke, & Garcés, 2010; Fee et al., 2013; Le Pichon et al., 2005; Liszka & Garcés, 2002; Matoza et al., 2017; Matoza et al., 2018; Matoza, Le Pichon, et al., 2011; Matoza, Vergoz, et al., 2011). Local infrasound networks (sources <15 km distant), however, are better placed for identifying smaller explosions, degassing, or effusive behavior within a limited radius (e.g., De Angelis et al., 2012; Fee et al., 2016; Fee, Garcés, et al., 2010; Johnson et al., 2003; Jolly et al., 2017;

Matoza et al., 2010; Petersen & McNutt, 2007). A dense regional seismoacoustic network such as the TA falls between these two endmember network geometries, affording an unprecedented opportunity to evaluate explosive volcanic eruptions, wave propagation, coupling, and signal evolution for source-sensor ranges out to a few thousand kilometers (e.g., study of the Pavlof March 2016 eruption by Fee et al., 2017). Regional infrasound coverage on a similar scale to the TA is currently limited to combinations of national networks such as those in the Euro-Mediterranean region (Tailpied et al., 2017). Other national infrasound networks include those in Iceland (Jónsdóttir et al., 2015), Japan (Batubara et al., 2018), Chile (Matoza et al., 2018), and Singapore (Perttu et al., 2018).

Regional-scale studies using seismoacoustic TA data have previously considered nonvolcanic events in the contiguous United States, with signals ranging from short and impulsive (e.g., de Groot-Hedlin & Hedlin, 2015; Edwards et al., 2014; Walker et al., 2011), to long and emergent (e.g., de Groot-Hedlin et al., 2014; Fan et al., 2018). Infrasound produced by explosive volcanism can be equally complex, from minutes to days in duration, with impulsive or emergent signals of time-varying frequency (e.g., Fee & Matoza, 2013; Johnson & Ripepe, 2011; Lees et al., 2004; Matoza et al., 2017; Matoza et al., 2019; Petersen et al., 2006; Ruiz et al., 2006). Here we describe how seismoacoustic signals from a range of Alaskan and Kamchatkan volcanoes are recorded on regional and seasonal scales and present a method derived from those observations for the detection, location, and characterization of these eruptions. We use existing volcano catalog information to validate our results and determine the capabilities and limitations of the method for this data set.

1.2. Monitoring Networks

This study incorporates data from regional seismoacoustic networks including the TA, those of the AVO and Alaska Earthquake Center (AEC), and local elements of the International Monitoring System (IMS) and Global Seismograph Network (Figure 1). Telemetered data sampled at 20 Hz and higher are available in real time for public download from servers operated by Incorporated Research Institutions for Seismology and the U.S. Geological Survey. Stations in these networks include both stand-alone seismic and infrasound sensors (Busby et al., 2018; USArray, 2019), as well as seven infrasound arrays (Lyons et al., 2020). AVO arrays are located at Adak, Akutan, Cleveland, Okmok, Sand Point, and Dillingham, with the Fairbanks array (IMS IS53) operated by the University of Alaska Fairbanks Geophysical Institute (Figure 1a). During the study period, there are up to 274 infrasound sensors from these networks within 3,000 km of Bogoslof volcano (Figure 1b). The term "array" is typically used for sensor geometries where signal wavelengths of interest (here, 1 km or less) are of the order of the sensor spacing (Havskov & Alguacil, 2016). To avoid ambiguity, hereafter "arrays" should be interpreted to mean only the AVO and IMS arrays, which have sensor spacing of 1 km or less. Stations in the TA will be referred to as single-sensor stations, which have typical sensor spacings of 85 km in Alaska.

1.3. Bogoslof Volcano Eruption

The 2016–2017 eruption sequence of the remote Bogoslof volcano, Alaska, provided a unique data set for developing and testing our algorithm. Seventy distinct eruptive events were characterized by AVO between 12 December 2016 and 30 August 2017, using a combination of geophysical data at local AVO stations (within 900 km), satellite images, lightning records, and eyewitness accounts (Coombs et al., 2019). The vast majority of these eruptions produced detectable infrasound, which, depending on event size, vent exposure/submersion, and atmospheric conditions, is observed at distances of up to 2,000 km or more (Figure 2). Infrasound signal durations lasted from minutes to hours, with infrasound frequencies extending from below 0.1 Hz to more than 10 Hz (Lyons et al., 2019, 2020; Fee et al., 2020; Schwaiger et al., 2020). The AVO eruption chronology catalog (Coombs et al., 2019) represents the best possible record of Bogoslof activity, and thus provides a metric by which to test our trial detection algorithms. Additional seismoacoustic studies of Bogoslof using proximal stations include those by Tepp et al. (2020), who characterize seismic and hydroacoustic data from swarms and eruptive activity; Haney, Van Eaton, et al. (2020), who describe thunder and electromagnetic signals produced by volcanic lightning from Bogoslof; Wech et al. (2018), who incorporate hydroacoustic T phases to model magma intrusion and eruption dynamics; Fee et al. (2020), who examine the relation between vent submersion and seismoacoustic ratios; and Lyons et al. (2019), who model low-frequency infrasound signals as giant, explosion-driven gas bubbles. Details of historical eruptions and hazards at Bogoslof are given by Waythomas and Cameron (2018) and Waythomas et al. (2020).

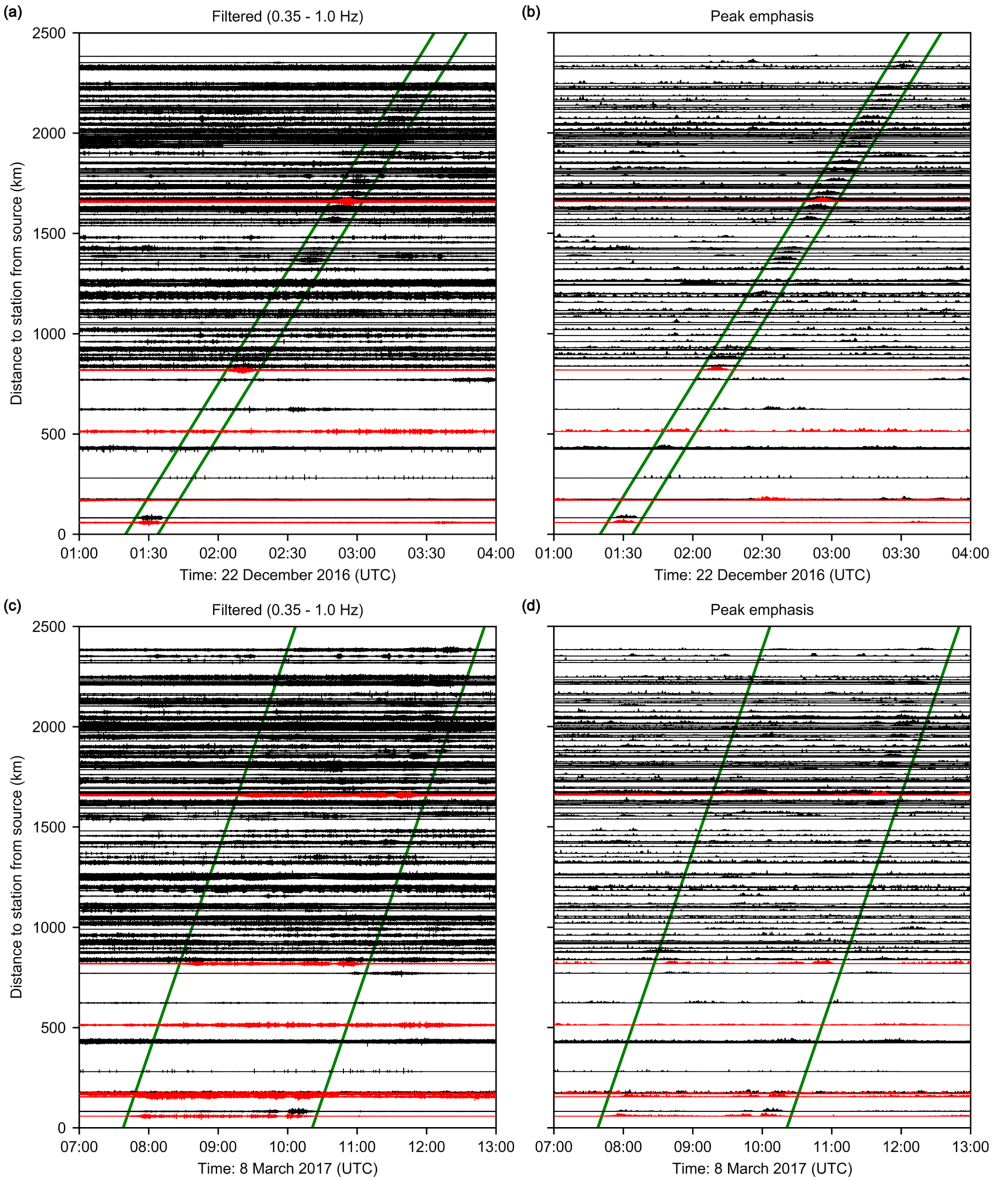

Figure 2. (a) Infrasound record section for Bogoslof eruption on 22 December 2016 using data filtered 0.35–1.0 Hz. The 14-min event signal is enclosed by diagonal green lines (celerity: 315 m/s). Traces for array sensors are colored red, and nonarray sensors colored black. (b) Traces from (a) following all data preprocessing stages which increase interstation event coherence (section 2.2). (c and d) Record sections for 8 March 2017 eruption. Event signal ~2.5 hr; best fit celerity: 280 m/s. Other details per (a) and (b). Although both these events are relatively large for the Bogoslof eruption sequence, sensors may not always record clear event arrivals due to atmospheric propagation paths and/or wind noise.

2. Methodology

2.1. Reverse Time Migration Overview

Reverse time migration (RTM) is a method for acoustic signal source localization; it is a time domain back-projection technique that identifies potential locations as those with the largest corresponding stack amplitude of waveform envelopes time-aligned with an appropriate velocity model. RTM has been used with seismic data (e.g., Arrowsmith et al., 2018; Shearer, 1994; Xu et al., 2009), as well as infrasonic ground-coupled airwaves (e.g., Walker et al., 2010, 2011, with TA data). Alternatives to RTM have been proposed for seismoacoustic event location with TA data; for example, de Groot-Hedlin and Hedlin (2015, 2018) and Park et al. (2018) employed a mesh of subnetworks in an array processing scheme. Other recent

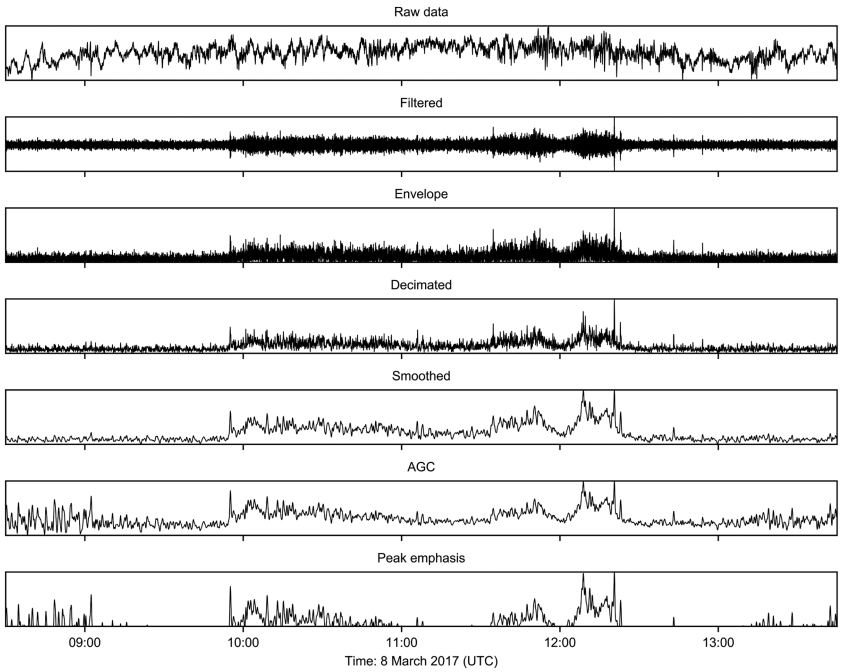

Figure 3. Sequence of the main preprocessing steps (going from top to bottom) for infrasound data recorded by station TA.N32M, located 2,210 km from Bogoslof at Quiet Lake, Yukon, Canada, on 8 March 2017.

methods for locating volcanic infrasound using combinations of single sensors are available (e.g., Jones & Johnson, 2011; Kim & Lees, 2015; Pinsky et al., 2017; Szuberla et al., 2006). Here we choose to evaluate the ability of RTM to provide coarse initial locations as starting points for more accurate techniques and for near-real-time operation at remote distances (<2,000 km) from the source. Our approach builds upon the formulation of Walker et al. (2010, 2011), who applied RTM over a large grid (western United States) for a range of celerities (defined as the total distance along the Earth's surface, or range traveled, divided by the travel time). To develop our algorithm, we use data from 15 December 2016 to 14 January 2017. This period contains frequent Bogoslof explosions with a range of amplitudes and durations. Furthermore, stratospheric wind directions were typically toward the bulk of the network, thereby improving signal-to-noise ratios (SNR). The same algorithm is subsequently applied to all data from 1 December 2016 to 30 September 2017. All dates and times in this paper are in Coordinated Universal Time (UTC). Additional details about the various stages of our methodology are included in the supporting information.

2.2. Preprocessing of Data

Significant preprocessing of data is necessary to improve SNR and waveform coherency between stations. Our prestack processing performs the following steps for each sensor trace: (1) demean; (2) taper with a Tukey window (to reduce filtering artifacts); (3) filter with a zero-phase order-2 band-pass Butterworth filter 0.35–1.0 Hz (a balance between eruption signal and background noise); (4) form envelopes (to increase interstation coherence); (5) decimate to one sample per 5 s after applying an anti-alias filter (computational efficiency); (6) smooth with a Gaussian window of width 75 s and standard deviation 10 s (to further increase interstation coherence and reduce spatial aliasing); (7) detrend via subtraction of a running minimum function with a 7-hr low-pass setting, hereafter called *subtrending* and inspired by Blackburn (2015) (to reduce wind noise while avoiding filter artifacts); (8) apply automatic gain correction (AGC) using a 3,600 s window (to further suppress wind and emphasize weak signals under noisy conditions); (9) demean and set any negative values to 0 (to emphasize peaks); (10) normalize on a 0 to 1 scale (to avoid dominance by noisy stations and account for attenuation). Figure 3 illustrates the main preprocessing steps for a single trace from the 8 March 2017 Bogoslof event (Figures 2c and 2d).

As the preprocessing steps do not preserve signal shape, the resultant stack cannot be directly and quantitatively linked to source process and event size. However, in general, larger and more sustained volcanic

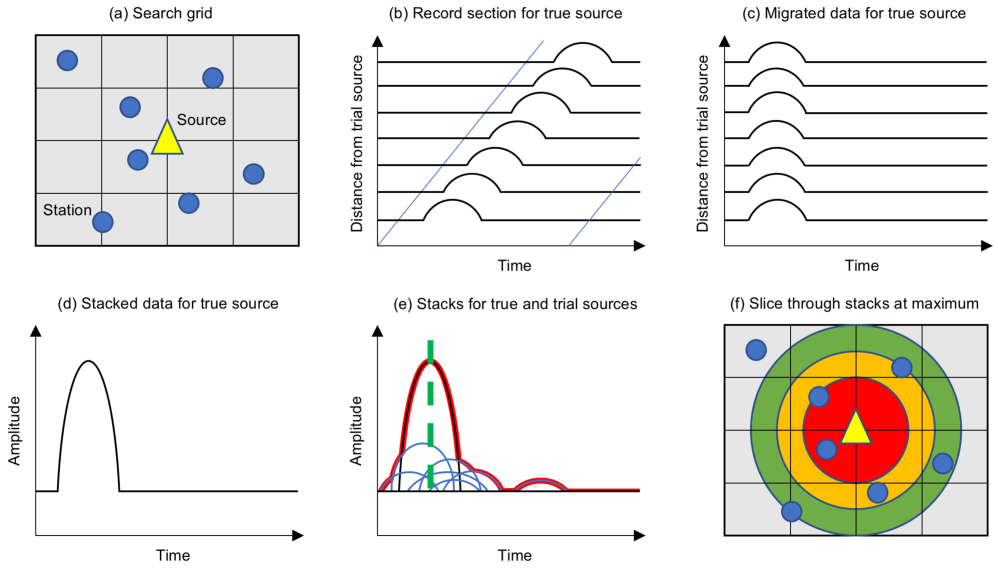

Figure 4. (a) Signal source and stations within a grid of trial source nodes. (b) Envelopes recorded by stations when using true source as the trial source. Data sections are extracted according to modeled celerity (diagonal blue lines). (c) Data sections from (b) are reverse migrated in time to the projected origin time. (d) The migrated data are stacked. (e) Stacks for all grid nodes. The stack for the true source (colored black) has the highest amplitude; stacks far from the true origin have small stacks (colored blue). A simple DF is the running maxima of all these stacks (colored red). The time of the DF maximum is marked with a green dashed line. (f) Contoured map of stack amplitudes at the time of the DF maximum in (e). Hotter colors toward the center are associated with stacks with higher amplitudes. Correct source locations are only provided by choosing times from (e) when the stack from the true source node is the highest.

explosive eruptions will produce higher SNR and longer-duration signals across more stations, resulting in higher stack values. Similarly, our location approach relies on increasing SNR through stacking rather than relying on the amplitudes of nonnormalized traces. Preprocessing generally improves the SNR of stacked data, but the degree of improvement varies with parameter choices and varies from event to event. For the example in Figure 3, the smoothing stage provides the clearest signal, but for other stations and events, this is typically not the case. Noise emphasized by AGC is less coherent across the network than signals from events and does not often stack constructively during RTM. The waveform data in this study are processed in nonoverlapping 24-hr sections, with additional data padding to accommodate all travel times.

2.3. Stacking of Data

We search for potential source locations across a 2-D spatial grid covering Alaska at 1.0° intervals in latitude and longitude. We test each grid node by delaying and linearly stacking waveform data from all sensors within 2,000 km of Bogoslof using 11 trial celerities, linearly spaced between 250 and 350 m/s (Figures 4a–4d). Rather than repeat the spatial grid search at a series of trial origin times, we treat the data samples themselves as a time grid, and the intersample spacing (5 s) as time windows. The grid search produces 11 sets of stacks, one set for each celerity. These 11 sets are then reduced to an adopted final set by retaining the highest stack amplitude at each time step (Walker et al., 2010, 2011); this is analogous to the beamforming approach of, for example, Green and Nippress (2019). Before and after the celerity set reduction, the stacks for each grid node are subtrended with a 6-hr low-pass setting. Applying these detrending steps here produces higher SNR than if applied in subsequent steps, and also ensures similar background amplitudes when concatenating multiple data sections.

Although infrasound for some Bogoslof events is detected to more than 2,000 km (Figure 2), we limit the station radius for this study to 2,000 km to preserve detectability for small events from Bogoslof, while retaining the bulk of stations. For RTM, including data from more sensors in the stack does not necessarily improve SNR and can worsen it as more noisy traces are added; this can be exacerbated by coherent noise and certain network geometries (Koper et al., 2012).

We treat the data from each sensor in an array as an individual contribution to the stack, rather than beamforming the array elements together to produce a single waveform for the array. Furthermore, in contrast to other backprojection studies (e.g., Walker et al., 2010; Xu et al., 2009), we do not apply any trace weighting based on sensor spacing. The rationale is that the sensors closest to each other (i.e., those at arrays, rather than single-sensor stations) are also those with the best wind-noise-reduction systems. Effects of different station subsets are explored in section 3.3.

2.4. Event Detection Method

Identifying and locating events in the stack requires stack metrics that provide an optimal balance between detecting volcanic events while minimizing false positive signals. This process begins by using a detector function (DF) in order to identify events (Arrowsmith et al., 2018; Walker et al., 2010, 2011). The DF shown in Figure 4e is simply a time series made up of the maximum amplitude of stacks. High DF values result from higher SNR signals across more sensors. Source locations are defined by regions with spatially coherent and high DF values (Figure 4f).

We refine this DF approach for volcanic eruptions, which can differ significantly in signal character from event to event and station to station. Importantly, variability in eruption durations (from minutes to hours) means that signals cannot be decimated to single impulses (a method employed by Walker et al., 2010, 2011). However, such expected properties of volcanic signals can be exploited to enhance detection using a regional-global network (Matoza et al., 2017). Here we specifically take advantage of the extended-duration signal property by using a summation window to increase SNR and simultaneously reduce the prevalence of artifacts and short, nonvolcanic signals. Due to this temporal summation process in forming the DF, the DF amplitude can be higher than the number of normalized waveform envelopes being stacked. The maximum possible DF value is the product of the number of traces and the number of time windows summed. We will continue to use *DF* when referring to this approach, or explicitly refer to it as a *time-summed DF* (TS-DF), to distinguish the method from the standard *single-time-window DF* (STW-DF) approach when needed. Similarly, we will use *stack* to indicate the time-summed stacks from which the DF is derived.

Event detection is performed on DF time series using a minimum threshold of 12.5 dB, which is the typical maximum background level for our data. DF samples above this detection threshold are grouped automatically into *peaks* (requiring a minimum gap of 1,800 s), which are then located automatically. DFs are converted to an SNR in decibel (dB) units using the following equation (adapted from Walker et al., 2010):

$$DF_{SNR} = 20log_{10}\left(\frac{|DF_{filt}|}{median\left(|DF_{filt}|\right)}\right),$$

where DF_{filt} is a DF that has been high-pass filtered above a particular period to remove the DF background offset. Here, to calculate DF_{filt} we subtrend with a 48-hr low-pass setting. All results in this paper derive from event detection and location on month-long time series, except when focusing on individual events. In such cases, we use 24-hr time periods instead.

2.5. Event Localization

We locate events based on spatial and temporal maxima in the RTM stacks, exploring two primary methods. Given that each sample in a DF is tied to a particular grid location, simply taking the maximum value of a peak in the DF provides a nominal event location (Figures 4e and 4f). We define the resulting distance between the calculated and true location as the *mislocation*. However, in some cases there is no clear maximum to the peak, while the derived source location may be offset due to atmospheric propagation artifacts (section 3.6). Furthermore, as the shape of the peak is dependent upon network geometry, choosing the median DF sample of the peak is not a robust approach. Consequently, we focus on two alternate strategies to locate events, each using a windowed section of the peak, rather than just one sample. For each peak, k number of DF_{SNR} samples above a location threshold (LT) are assessed, where LT is defined as the 75th percentile of the DF_{SNR} samples in the peak. The location methods applied to the corresponding time period are as follows: (i) *MAX* (maximum): for $DF_{SNR}(k) > LT$, the final location is the average of the locations corresponding to samples within ±75 s of the maximum amplitude; (ii) *COM3* (center of mass in three dimensions): the final location derives from the weighted-mean of all stack samples while $DF_{SNR}(k) > LT$.

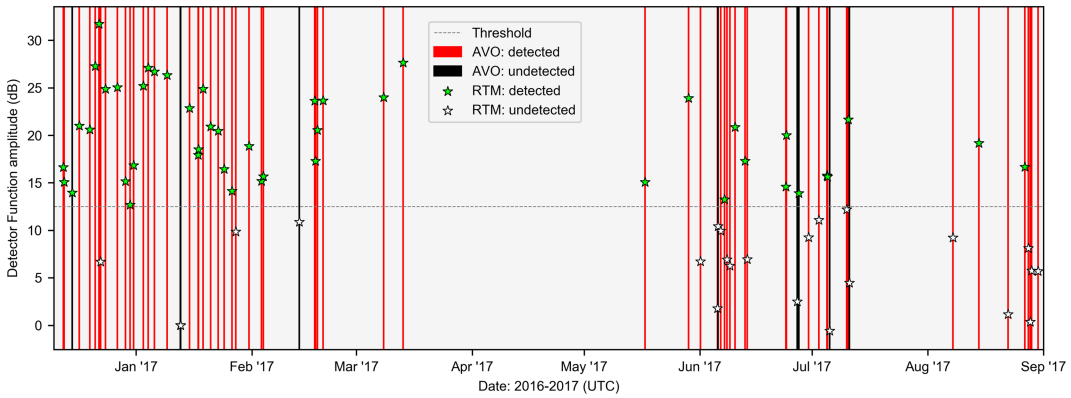

Figure 5. Time series of infrasound detection for the Bogoslof eruption sequence. Eruptions are marked by red lines if AVO registered infrasound for the events, and black if AVO did not (eruptions were confirmed through other data types). Similarly, events detected by RTM above the 12.5 dB detection threshold are marked with green stars, and events below this threshold are marked with white stars. The vertical scale represents the maximum amplitude of the DF within 15 min of the cataloged event.

3. Results

3.1. RTM of Bogoslof Eruption Sequence

For each Bogoslof explosion, detection of infrasound by AVO did not necessarily correspond with the start of eruptive activity, nor was infrasound observed for all eruptive activity (Coombs et al., 2019; Lyons et al., 2020; Schwaiger et al., 2020). AVO detected 61 of the 70 Bogoslof events with their infrasound array data (Figure 5, red lines) using analyses deriving from least squares beamforming (e.g., Lyons et al., 2020; Szuberla & Olson, 2004). When including all available sensors, our RTM method detects 44 of 61 of these cataloged infrasound events (72%, Figure 5, green stars), and 46 of 70 of the events as a whole (66%, Figure 5, white stars). Notably, our RTM implementation identifies two cataloged eruptions that were reported by AVO as having below-detection threshold levels of infrasound (22:10 14 December 2016 and 11:17 27 June 2017).

Monthly DFs for December 2016 to September 2017 are presented in section S3 of the supporting information. These figures include further details on AVO and RTM detections for each event. In addition to the confirmed explosions from Bogoslof, the DFs suggest additional events that were not cataloged. For example, on 11–12 January 2017, a relatively large peak in the Alaska-wide DF is observed, with the corresponding location less than 200 km from Bogoslof. However, as no AVO monitoring data types showed any volcanic activity (Coombs et al., 2019; Searcy & Power, 2020; Wech et al., 2018), we interpret this as a nonvolcanic infrasound source. Similar examples occur on, for example, 1, 9, 16, and 24 February 2017, several in April 2017, and also 24 July 2017.

3.2. RTM of 8 March 2017 Bogoslof Event

To illustrate the event detection and location procedure, we continue to focus on the 8 March 2017 eruption of Bogoslof. This event is of interest for being one of the largest across all of the monitoring categories used by AVO, including plume height, SO_2 mass, number of lightning strikes, event duration, and geographical range of seismoacoustic observations (Coombs et al., 2019). DFs for this event (Figure 6a, top panel) retain the two subpeaks broadly seen in Figures 2d and 3. With the chosen detection threshold, only the larger subpeak is automatically located. A lower threshold or manual analysis would allow for locating both subpeaks separately. Divergence of the Alaska-wide DF (colored) from the Bogoslof-specific DF (black) during the eruption is due to the contributions from stacks at nonsource grid nodes (as per Figure 4e). Changes in the mislocation value with time (Figure 6a, bottom panel) reflect the evolving location of these nonsource grid nodes in response to Alaska-wide infrasound sources.

A time slice through the stack information (Figure 6b) also shows the two location estimates for the event. The time of the map corresponds to that of the highest Alaska-wide DF amplitude (as per Figures 4e and 4f). The color scale represents the amplitude of time-aligned data stacks at each grid location. The MAX event location coincides with Bogoslof (zero mislocation), and the COM3 method locates the event 341 km SSW

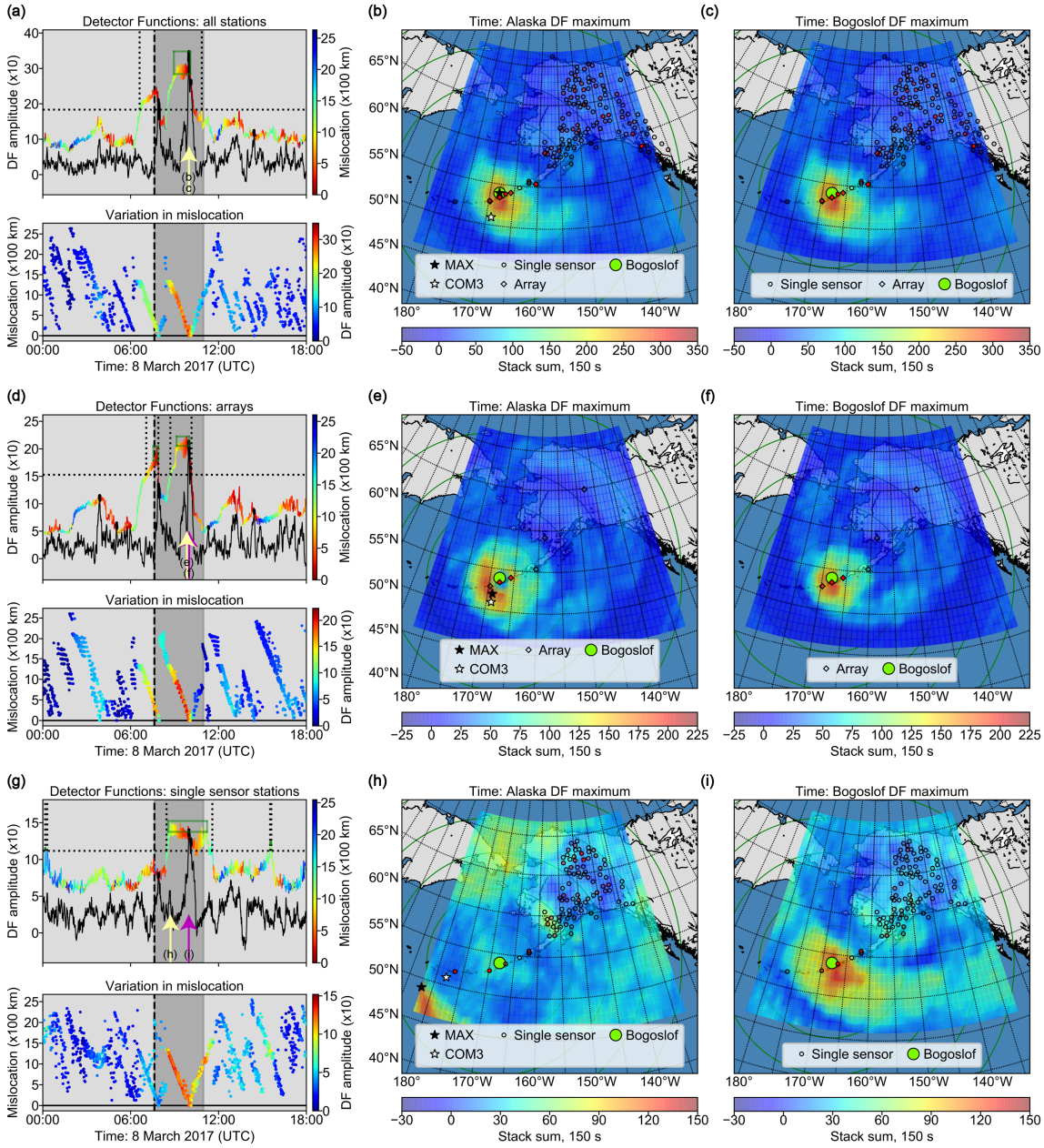

Figure 6. (a) Top panel: Alaska-wide DF (colored by mislocation) and Bogoslof-specific DF (colored black) for the 8 March 2017 Bogoslof explosion. The Bogoslof-specific DF is the stack corresponding to the trial source location (grid point) at Bogoslof. Matching amplitudes between the two DFs (marked with bold black line segments) indicate zero mislocation. Final location estimates for peaks are performed only on the high amplitude values boxed with solid green lines. Data are from all available infrasound sensors within 2,000 km of Bogoslof. The vertical dashed line is the AVO cataloged event onset, and the dark gray section the period of AVO cataloged infrasound. Dotted lines earmark samples above the 12.5 dB detection threshold. Bottom panel: Variation in mislocation from Bogoslof for each DF sample. (b) Time slice of results corresponding to larger subpeak in the Alaska-wide DF. The timestamp of the map is that of the DF maximum amplitude, marked by a yellow arrow in (a). The color scale represents the amplitude of time-aligned data stacks at each grid location. Locations provided by the MAX and COM3 methods are marked. Sensors are shaded red proportional to stack contribution for the corresponding source time. Circles are at 500 km spacing. (c) As per (b) but at the time of the maximum in the Bogoslof-specific DF. A purple arrow in (a) is typically used to mark the corresponding time; however, in this case the two map times are identical so the purple arrow is not distinguishable. (d–f) As for (a–c) but using data from only the infrasound arrays. (g–i) As for (a–c) but using data from only the single-sensor stations.

of Bogoslof. Sensor shading (red) is proportional to relative stack contributions assuming the MAX location is the true source. Such sensors comprise those in nearby arrays as well as several single-sensor stations to 2,000 km range with no clear distribution pattern. A time slice during the Bogoslof-specific DF maximum (Figure 6c) is identical to that of Figure 6b.

3.3. Subnetwork Influence

Here we assess the relative contributions to stacks from single-sensor stations and arrays in order to understand their respective impact. The first influential factor is proximity to volcanic sources. With infrasound arrays making up the majority of sensors within 900 km of Bogoslof (Lyons et al., 2020), these sites are nominally better placed to have higher SNR than stations at greater distance. Mitigating factors, however, include potential shadow zones within the first few hundred kilometers (Fee & Matoza, 2013, and references therein) and higher local wind noise away from the Alaskan interior. The second factor is mechanical noise suppression. Half of the sensors comprising the infrasound arrays in this study use physical noise canceling technology, such as wind domes (Lyons et al., 2020; Raspet et al., 2019; Walker & Hedlin, 2010). The TA stations in contrast, which make up the bulk of the single-sensor stations, do not use spatial wind filtering devices. The third factor is sensor separation. The seven arrays in our study contain between four (AVO OKIF) and eight (IMS IS53) sensors. Data recorded by each sensor in an array are typically highly similar because of their close proximity (tens of meters to a few kilometers depending on the frequency range of interest). Hence, stacked envelope data for a single array will provide a higher SNR compared to an equal number of nonarray stations.

Array and single-sensor station results for the 8 March 2017 event are compared in Figure 6. For the array data, the two subpeaks (Figure 6d) are similar to those of the combined station data (Figure 6a). The MAX location for the second subpeak here has a mislocation of 233 km (Figure 6e), compared to no mislocation when using all sensors. In contrast, the single-sensor DF has a low SNR, and does not resolve the first subpeak (Figure 6g). Further, the location estimates for the second subpeak (Figure 6h) are highly inaccurate. This occurs because the relatively high samples in the Alaska-wide DF represent grid nodes far from Bogoslof. Accurate automated locations are only obtained if the highest Alaska-wide DF amplitudes are from stacks for grid nodes close to Bogoslof (e.g., Figures 6a–c). The absolute prominence of the Bogoslof-specific DF in Figure 6g, or its similar appearance to those in Figures 6a and 6d is therefore not a factor in event localization. Rather, the relative amplitudes of the Bogoslof and Alaska-wide DFs are important. More accurate locations for the single-sensor station example would be provided by automated or manual selection of DF samples when the Alaska and Bogoslof DFs intersect at ~09.45 (Figure 6i). Animations showing the time-evolution of Figure 6 are provided in the supporting information as Movies S1–S3.

The relative location accuracy of the three station groupings is in part a consequence of the source-station geometry, with the single-sensor stations having the lowest azimuthal coverage of Bogoslof. Hence with the addition of noise, and increased wavefield dispersion with source-receiver distance (e.g., Green & Nippress, 2019), stacked data at grid nodes other than the true source may have the highest amplitudes (Figures 6h). This scenario is reflected by the contrast in mean mislocation for the background/nonevent DF samples in Figures 6a, 6d, and 6g (bottom panels). The array-only data (Figure 6d) have a majority of location values close to Bogoslof, whereas the single-sensor station data (Figure 6g) have typical mislocations of 1,000–2,000 km, reflecting grid nodes in mainland Alaska. Therefore, for stations with good azimuthal coverage of the source, or for stations that are close to the source, selecting nonoptimal DF samples can still give a reasonable position (Figures 6b and 6e). The 15 January 2017 Bogoslof eruption is another event widely recorded across Alaska (Figure 7). In contrast to the 8 March 2017 event (Figure 6), here, each of the three groups of stations under consideration locate the event more similarly.

Given the anticipated effects of seasonal stratospheric wind direction on signal detection (Le Pichon et al., 2009), Figure 8 explores how the Alaska-wide DF maxima for AVO-cataloged infrasound events varied during 2016–2017. We compare results from single-sensor stations and arrays, as well as account for the number of sensors in operation. DF amplitudes for both data sets are lower for June through August 2017 (Figures 8a and 8b) compared to earlier in the year, despite the increase in installed sensors. Figure 8c shows that in relative terms, there is a positive relation between sensor contributions to DFs for either station category. In absolute terms, the array sensors contribute more to DFs than single sensors. For both data sets, the DF contributions per sensor are higher from December to March, than June to August. A switch in stratospheric wind direction from eastward to westward over the time period does not, however, preferentially affect one set of stations over the other, despite the arrays having better azimuthal coverage of Bogoslof (Figure 1a). Detailed analysis of atmospheric behavior during the Bogoslof sequence is provided by Schwaiger et al. (2020).

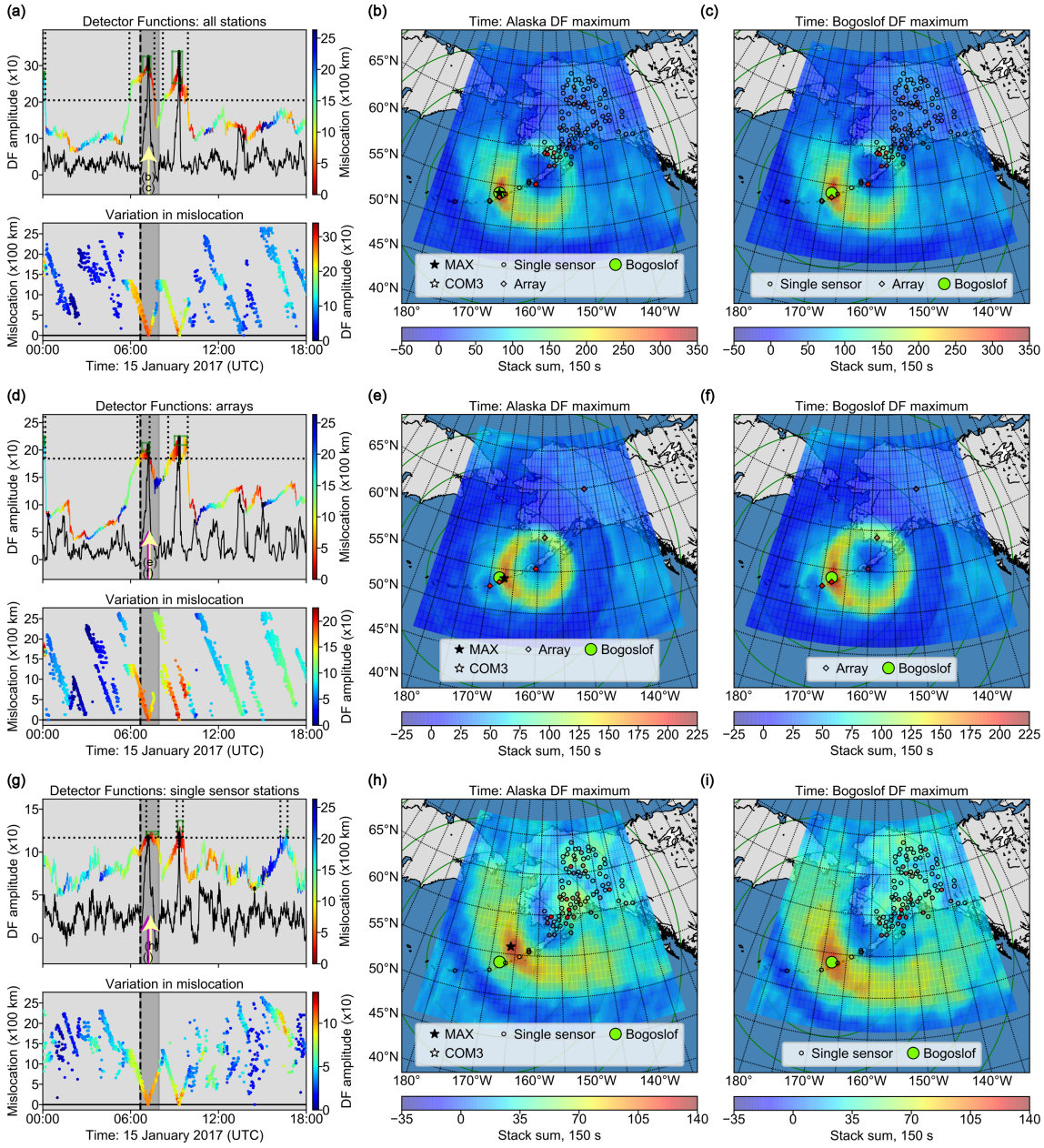

Figure 7. As for Figure 6 but using data from the 15 January 2017 Bogoslof eruption. Each map plots the location for the first peak, which has AVO cataloged infrasound, whereas the second peak does not have such information. In each case, the MAX and COM3 location estimates are colocated. The event locations from each sensor grouping are relatively similar compared to those in Figure 6.

Accounting for event size in the observations from Figure 8 is challenging as independent metrics of volcanic intensity such as plume height, SO_2 mass, and number of lightning strikes (Coombs et al., 2019), do not robustly correlate with infrasound signal characteristics (e.g., Lopez et al., 2020). A particular complication in this regard is accounting for the fluctuating vent conditions (submarine to subaerial), dome building activity, and any cloud coverage which hampers satellite observations. Given these constraints, however, no particular decrease in event magnitude is identified over the course of the eruption. Similar event size comparisons exist for precursory seismicity (Tepp & Haney, 2019), and eruptive seismicity (Haney, Fee, et al., 2020; Tepp et al., 2020).

3.4. Algorithm Performance for Bogoslof Eruption Sequence

We use receiving operator characteristic (ROC) curves (Fawcett, 2006) to compare the ability of different RTM algorithms to correctly classify events. These ROC curves plot the true-positive rate (TP rate) versus

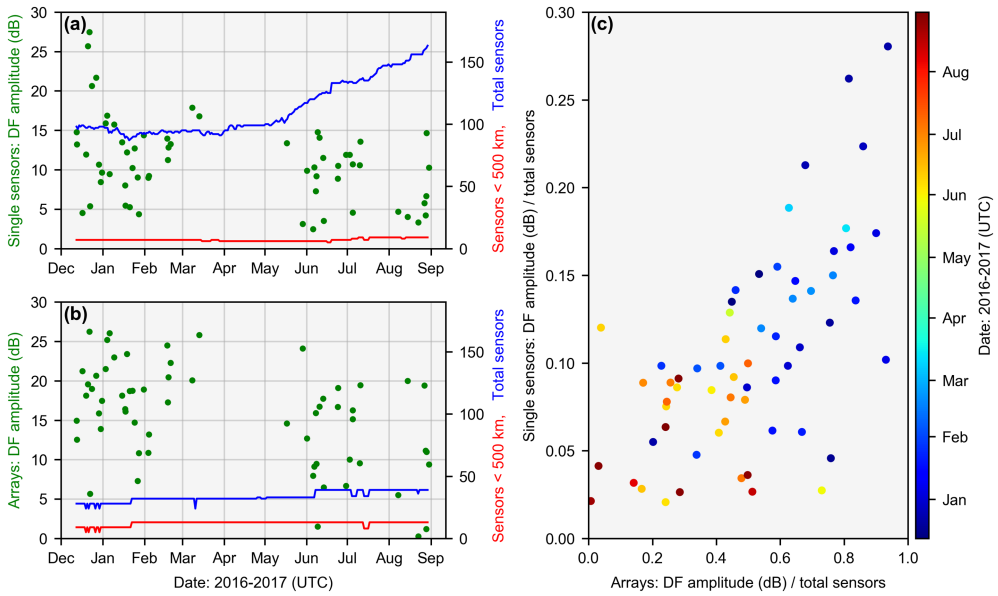

Figure 8. (a) Single-sensor station DF amplitude (in dB) and sensor number versus time, for infrasound-generating events cataloged by AVO (±15 min). Sensor quantity is shown for both total sensors (blue line) and sensors within 500 km of Bogoslof (red line). (b) As per (a) but for arrays. (c) Sensor contribution to DFs in absolute and relative terms for the arrays and single-sensor stations, shaded by time.

false-positive rate (FP rate) of a DF for a range of detection thresholds (Figure 9). An algorithm that classifies events perfectly will have a threshold that gives a TP rate of 1, and an FP rate of 0. For such an algorithm, the area under the curve (AUC) accounts for 100% of the total possible area. AUC values close to 50% are equivalent to classifications being a random guess. A ROC curve is equivalent to plotting the probability of an eruption versus the probability of a false alarm. We automatically classify detections by comparing AVO infrasound catalogs for Bogoslof to DF samples at equivalent times, on a sample by sample basis. Other volcanic events such as those from Cleveland are not treated as cataloged events, nor are known nonvolcanic events. ROC calculations are performed on month-long DF_{filt} time series.

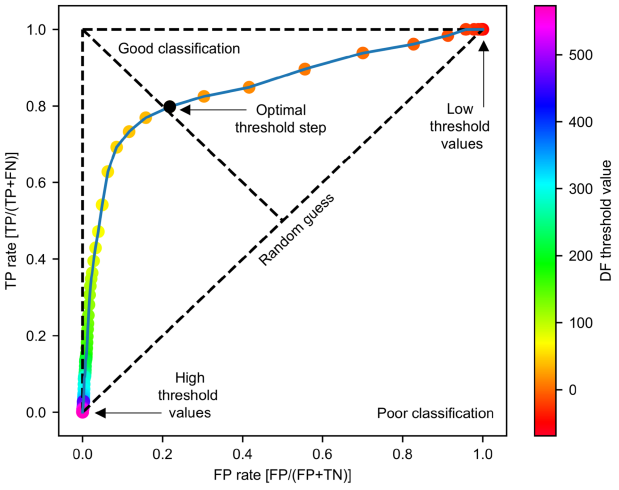

Figure 9. ROC curve for December 2016 data. A DF detection threshold of 29.4 gives a moderately high TP rate (~0.8) and moderately low FP rate (~0.2). The area under the curve (AUC) is 85%. TP, true positive = eruption with DF > threshold T; FP, false positive = no eruption with DF > T; TN, true negative = no eruption with DF < T; FN, false negative = eruption with DF < T.

ROC curves are also useful for comparing RTM parameter choices, station choices, and time of year, all factors which can affect the SNR of DFs (Figures 5 and 8). For instance, to further illustrate seasonal weather influences for the three station groups, Figure 10 compares ROC results for each month using AUC as a classification metric. Figure 10 also compares implementation of the TS-DF and STW-DF approaches to assess if there are differences in classification performance between the two methods. We find that for both DF formats, AUC values are typically at or above 75% for the majority of the year. Only July and August 2017 have AUC values close to 50%. The classification performance for the single-sensor stations is poorer than the other two station configurations. Overall, TS-DFs classify volcanic events marginally better than STW-DFs.

We also evaluate seasonal effects on algorithm performance over the Bogoslof eruption sequence by plotting (1) the percentage of AVO cataloged infrasound events detected by RTM (allowing a ±15-min margin), and (2) the location accuracy of those detected events using monthly averages (Figure 10). As with the ROC classification performance, the event detection rates and location accuracy are typically better from December 2016 to May 2017, and poorer subsequently. Notable differences between the DF methods include STW-DFs being relatively strong for event detection rates (up to 85% overall), with the greatest difference

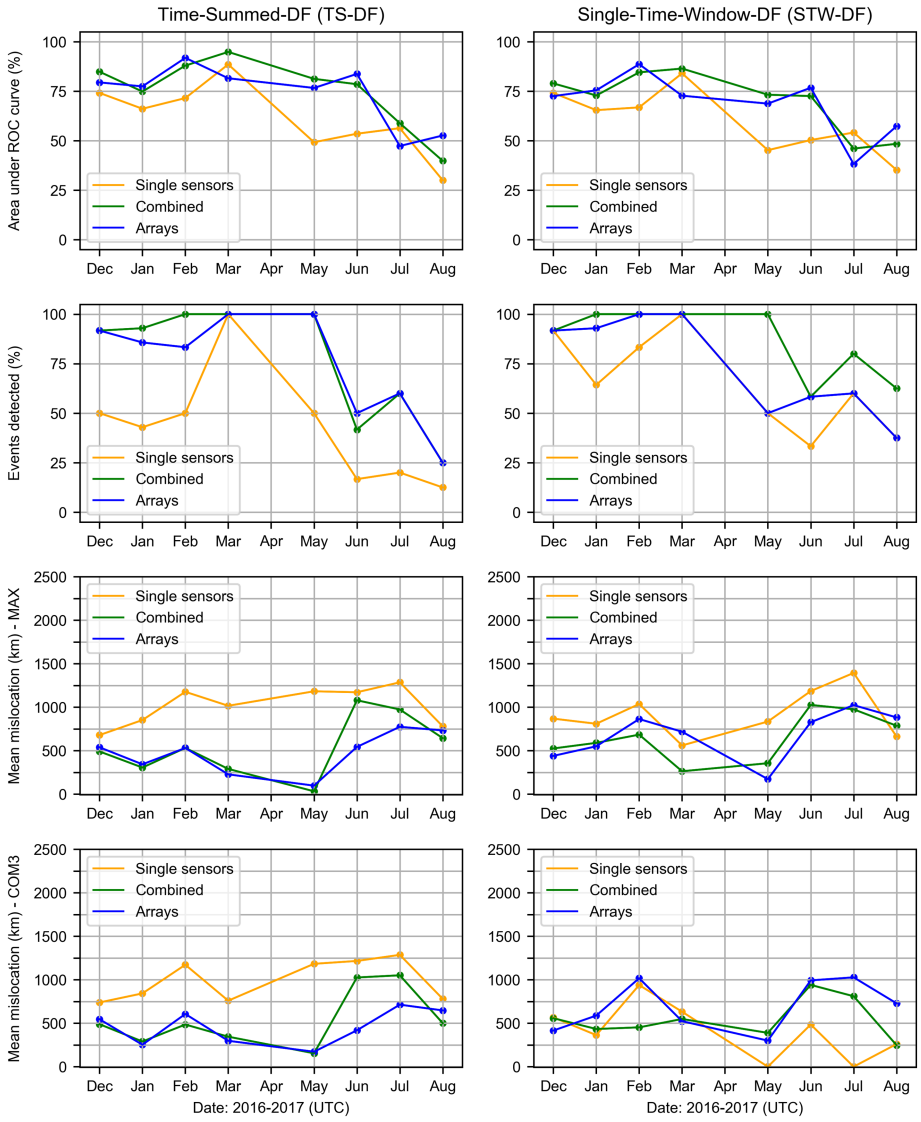

Figure 10. Comparison of detection and location results using TS-DF (left column) and STW-DF (right column) approaches. Though broadly similar, the TS-DF method, as used throughout the paper, is relatively strong for array-only stations versus single-sensor stations, whereas the STW-DF is particularly advantageous for single-sensor station and combined sensor results in terms of event detection. Bogoslof events were cataloged by AVO for every month except April 2017. Absence of markers for a particular month here indicates no detections by the method.

being for the single-sensor stations. Similarly, for the location methods, STW-DFs perform relatively well for the single-sensor station data, though direct comparison is challenging given the contrasting event detection rates.

3.5. Algorithm Performance for non-Bogoslof Events

Since the beginning of the Bogoslof eruption sequence in December 2016, many other volcanoes in the North Pacific have erupted. The volcanoes from Alaska are: Cleveland, Great Sitkin, Semisopochnoi, and Veniaminof (Figure 1) (Alaska Volcano Observatory, 2019), and from Kamchatka: Bezymianny, Ebeko, Kambalny, Karymsky, Khangar, Klyuchevskoy, Koshelev, Sarychev Peak, Sheveluch, Zheltovsky, and Zhupanovsky (KVERT, Institute of Volcanology and Seismology FEB RAS, 2019). We assessed a subset of these (Table S2 of the supporting information) based on network proximity, event size, and plume direction. Of the Alaska events, only the Cleveland explosions are clearly detected by RTM (using the same parameter

set for Bogoslof). These results are somewhat expected as most of the nondetected eruptions were relatively small. Of the five Kamchatka events focused on, only the Bezymianny explosion on 20 December 2017 is clearly identified. Candidate events from near Koshelev and Zheltovsky are suggested by RTM but these do not match events in KVERT catalogs. Unfavorable propagation and attenuation conditions may explain the lack of clear observations from nondetected Kamchatka events, which were on a similar scale to that of Bogoslof on 8 March 2017. Detection performance for eruptions in Kamchatka and the western Aleutians could increase with inclusion of data from the IMS stations in Kamchatka (IS44) and others in the northern Pacific region (Fee, Steffke, & Garcés, 2010; Matoza et al., 2017), as well as any local infrasound networks in those areas (Gordeev et al., 2013; Matoza et al., 2019).

Additional nonvolcanic events are regularly seen in our DFs (section S3, supporting information). The IMS IS53 array in central Alaska is particularly well positioned to record urban noise, industrial and military blasts (Gibbons et al., 2019; Schneider et al., 2018), and rocket launches (de Groot-Hedlin et al., 2008) from the Poker Flat Research Range. Many of these types of events, and others such as debris flows (IRIS DMC, 2014; Toney et al., 2019) and bolides (Edwards et al., 2014; Walker et al., 2010), were recorded by the TA while it was traversing the continental United States. Such observations are detailed in the TA Infrasound Reference Event Database (de Groot-Hedlin & Hedlin, 2015; IRIS DMC, 2012). Several M6+ earthquakes in Alaska were also located by applying our RTM algorithm to air-coupled ground waves (also see Shani-Kadmiel, Assink, Fee, et al., 2018, and a review by Mikumo & Watada, 2010).

3.6. Source Resolvability and Stack Artifacts

The stacked data here contain significant artifacts, manifesting as event data being smeared across space-time in a phenomenon known as *swimming* (e.g., Meng et al., 2012). A correctly tuned RTM algorithm should generate event-based stack maxima only at the physical source, rather than earlier or later along a swimming track. Swimming is clearly apparent in Figures 6 and 7 by comparing the widths of peaks in the Alaska-wide and Bogoslof-specific DFs, as well as by observing the evolving mislocation during the event. Movies S1–S3 show this migration particularly well prior to, during, and after the 8 March 2017 event. Swimming is principally a consequence/function of the network geometry's response to a series of impulses (Koper et al., 2012). The artifacts are emphasized where sources are complex and outside the majority of the network (due to poor azimuthal coverage). Consequently, there are implications for being able to clearly resolve and accurately locate a source using stack information even under ideal atmospheric propagation and noise conditions.

To illustrate the impact of network geometry and source type further, Figure 11 compares synthetic sources (1- and 10-min durations) at three locations across the north Pacific. These locations represent sources within the network center (Fairbanks, Alaska), network margin (Bogoslof, Alaska) and far outside the network (Bezymianny, Kamchatka). During each DF shown, the stack for each true source is only represented briefly at time 00:00. For shorter impulse sources (Figure 11a), DFs at all three source locations have larger oscillations and generally clearer peaks than for longer, emergent sources (Figure 11b). These oscillations are simply the original source information stacking at non–true grid nodes with lower amplitudes. As the source duration grows (and/or grid spacing decreased), these peaks merge together. Relatively clear DF peaks occur for sources closer to the network center due to improved azimuthal coverage. Further, peak sharpness is also celerity dependent—the narrower the celerity search range, the narrower the DF (Figure 11 uses a single celerity of 300 m/s for simplicity).

Figures 11c and 11d show the stack information at time 00:00 in map form. Here, RTM location estimates are reflected by the intersection of ring features around individual sensors. When particular sensors contribute heavily to the location, the rings centered on those sensors are more pronounced. Such features are commonly seen around arrays which contain multiple equally weighted sensors, for example, Figure 7 and Movies S1–S3. Figures 11e and 11f plot cumulative stack amplitudes, illustrating the swimming tracks along the respective source-station axes. Stacked energy is more concentrated for short events and for source proximity to the network center, providing higher location resolution. The azimuthal coverage of these sources has parallels to how the groupings of combined, array, and single sensors are positioned in relation to Bogoslof.

The swimming artifact for the 8 March 2017 Bogoslof event is explicitly illustrated by Figure 12. The DFs in Figure 12a are the same as those from Figure 6a, but here the time slice map (Figure 12b) corresponds to the

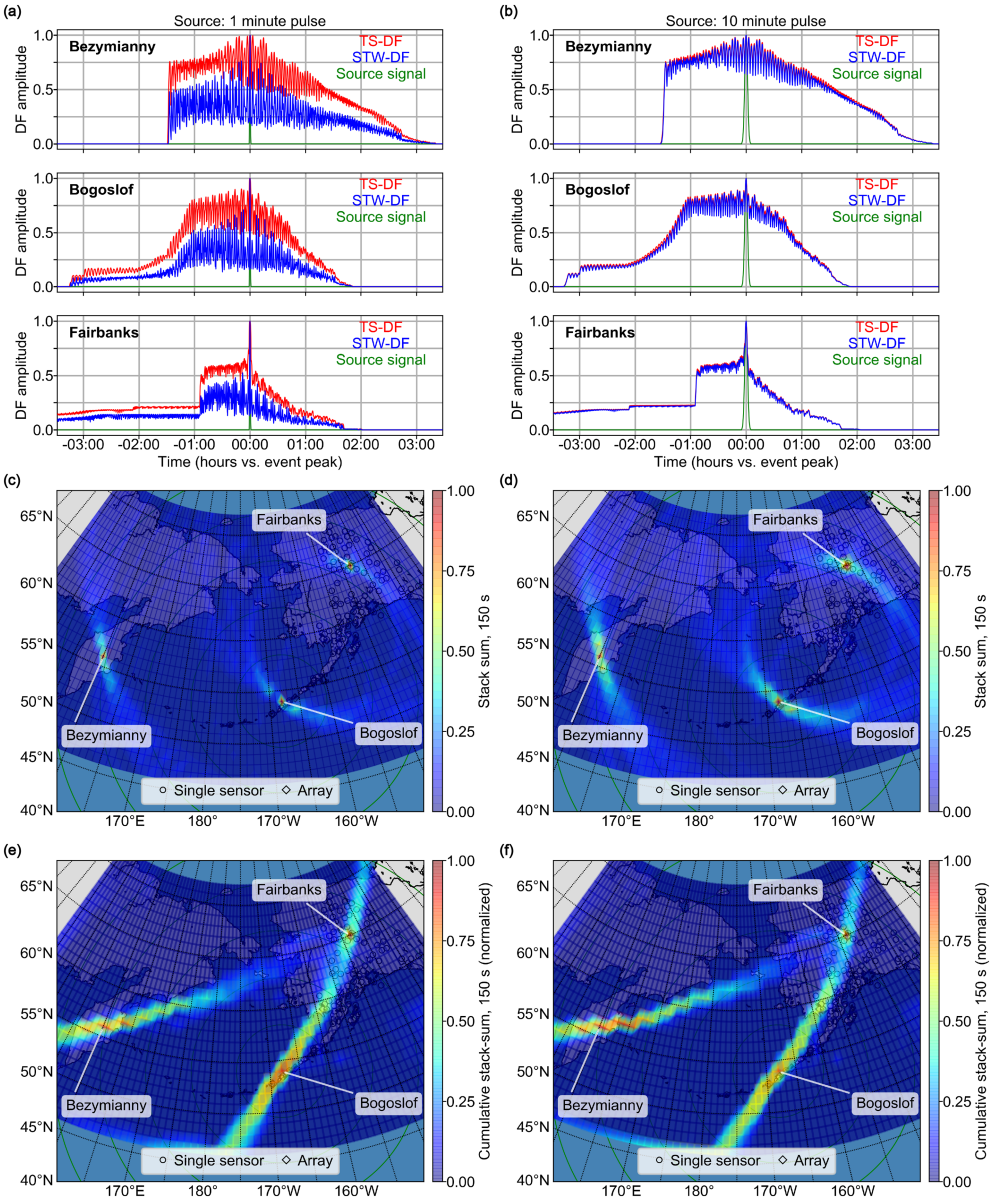

Figure 11. (a) Normalized DFs for a 1-min synthetic Gaussian source pulse, placed at three locations and propagated to all marked stations with a 300 m/s celerity. Sharp steps in the Bezymianny and Fairbanks DFs are a result of proximity to the grid boundary. (b) As per (a) but with 10-min Gaussian source pulse. (c, d) Maps showing time slices through time-summed stack data at times 00:00. Rings are at 500-km intervals. (e, f) Maps showing cumulative time-summed stack values at each grid node for the 1- and 10-min pulses.

maximum amplitude of the first, smaller subpeak of the Alaska-wide DF, rather than the second. The location of the highest stack energy is to the SW of Bogoslof, rather than at the true source. For subsequent time slices, the region of maximum stack energy migrates NE, passing Bogoslof at 07:53 (Figure 12c). A similar migration is observed for the second subpeak from 08:30–11:00. Figure 12d shows the cumulative stack amplitude at each grid node for the time period covering both DF subpeaks (06:00–12:00). Though the highest cumulative amplitude is at Bogoslof, there is significant energy distributed elsewhere. In particular, the SW corner of the grid accumulates amplitude values that would otherwise locate SW of the grid edge if it were not for this boundary. Consequently, the corner node is masked here to avoid dominating the color scale.

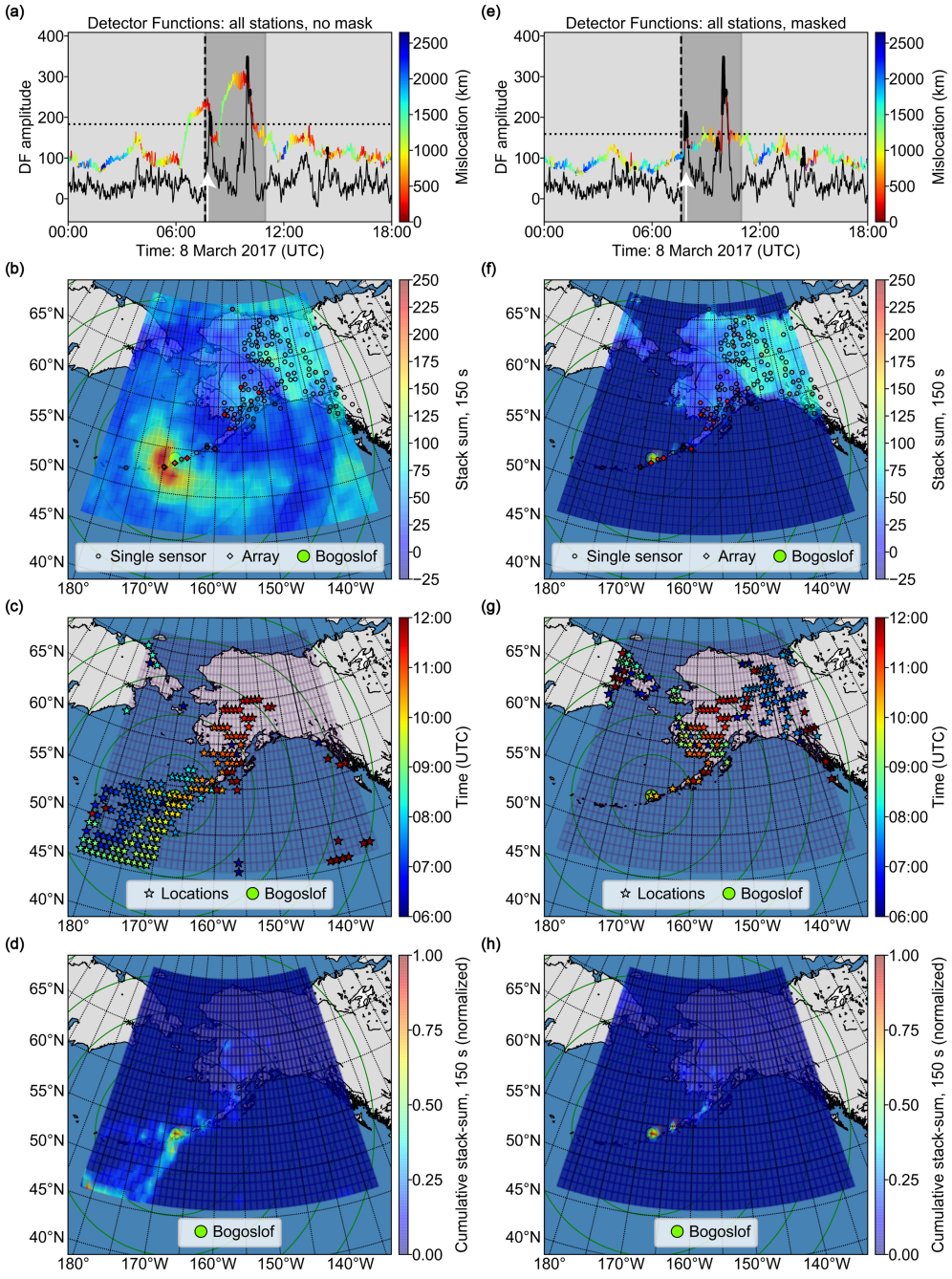

Figure 12. (a) DFs for the 8 March 2017 explosion from Bogoslof without a mask. Other details per Figure 6a. There is no mislocation of the maximum of the larger subpeak. The mislocation of the maximum of the smaller subpeak is ~200 km, however. (b) Time slice map corresponding to maximum of smaller subpeak (marked with arrow in Figure 12a). Other details per Figure 6b. (c) RTM locations for each sample in the Alaska-wide DF (Figure 12a), color-coded by time. (d) Location data from the Alaska-wide DF is binned by grid node and tallied. (e–h) As for (a)–(d) with a mask applied such that the DF is formed only from stacks for grid nodes close to land.

Limiting the grid search (or DF components) to nodes that are on land is a potential approach for mitigating swimming artifacts applicable to arc volcanism. Given the direction of swimming here is from SW to NE, the initial swimming artifact is entirely over the ocean until the Aleutian Islands are reached. By excluding grid nodes over the ocean, this preartifact can be removed from the DF, though postartifacts remain due to the remaining land (Figure 12e). Locations for the first subpeak are now accurate compared to without the

mask (Figure 12f vs. 12b). The evolution of mislocation with time also becomes unclear (Figure 12g) and the cumulative stack energy now shows a constrained distribution (Figure 12h). More severe masks could be used in order to restrict DFs to particular regions of interest (indeed the Bogoslof-specific DFs are an extreme case of this). Notably Landès et al. (2012) take the opposite approach whereby grid values over the continents are masked to avoid locating microbaroms on the continents. Arrowsmith et al. (2018) describe a range of related methods.

Other strategies to minimize or account for swimming include time-frame averaging (Koper et al., 2012), reference windows (Meng et al., 2012), as well as combining results from azimuthally distinct subnetworks, and exotic stacking techniques (e.g., Xu et al., 2009 and references therein). In evaluating three such stacking methods (*N*th root, semblance, and *F* ratio) we find that though swimming artifacts improve in some cases, in other cases the artifacts remain. Use of azimuthally distinct subnetworks for this study is problematic given the progressive deployment of the TA during the Bogoslof eruption. The westernmost stations (well placed to constrain events) were only deployed at the end of the eruption (Figure 1).

4. Discussion

Bogoslof was a complex seismoacoustic source, with the vent submerged for most of the nine-month eruption, impacting acoustic coupling with the atmosphere (Godin, 2008; Ichihara et al., 2009; Lyons et al., 2019, 2020; Fee et al., 2020). Infrasound from some explosions is detectable at ranges of 2,000 km or more by regional networks (Figure 2). Distant arrivals are sometimes clearer than those more proximal due to refractive shadow zones and atmospheric waveguides (Drob et al., 2003). The dense regional network in Alaska is, despite poor azimuthal coverage of the Aleutian Arc, capable in principle of identifying and locating explosions to subdegree accuracy using RTM. However, detection and location capability depends upon the number of arrivals, their azimuthal distribution, SNR, and processing methods.

One demonstrated shortcoming of RTM, though not unique to it, is that for sources outside the network, the location estimate has a spatiotemporal error ellipse along the source-network axis (Cochran & Shearer, 2006), manifesting as swimming artifacts (Figures 6, 7, 11, and 12). These artifacts result in locations for both background and high-amplitude DF samples migrating over the grid space. Thus, having an event trigger based only on whether a volcano-specific DF matches the Alaska-wide DF will have many false alarms, even during background noise. Without adequate azimuthal coverage of the source, a DF amplitude threshold is an insufficient control to resolve this issue (Figure 11). The majority of volcanoes of interest in Alaska are outside the margins of the bulk of monitoring stations, and consequently incorporation of an independent location estimate provided by local infrasound arrays would provide this azimuthal control. These arrays can provide individual back azimuths (Fee et al., 2016; Fee, Steffke, & Garcés, 2010; Gibbons et al., 2005; Iezzi et al., 2019; Le Pichon et al., 2005; Ripepe et al., 2007), and distances (Green & Nippress, 2019; Shang et al., 2019; Shani-Kadmiel, Assink, Smets, et al., 2018; Szuberla et al., 2006), in addition to source triangulation through a cross-bearings approach (e.g., Le Pichon et al., 2008; Matoza, Le Pichon, et al., 2011; Matoza, Vergoz, et al., 2011; Mialle et al., 2015; Matoza et al., 2017). The relative consistency with which stacked array data characterizes eruption records, when compared to a network of single sensors demonstrates the importance of these arrays. Similarly, deriving locations by treating the existing network as a mesh of three-station triads is another approach (de Groot-Hedlin & Hedlin, 2015).

The success of the RTM method also depends on the alignment and shape of envelopes being stacked. For instance, events tend to locate well if the original waveforms have features that are sharp/impulsive enough, or can be processed in such a way that a DF reflects that sharp feature (Figure 7). The contrary is also true—broadly topped DFs may not locate well, particularly if the DF maximum is taken arbitrarily (Figures 6g and 6h). An important related factor is that RTM stacks energy rather than phases, and thus stack amplitudes and the ability to locate an event are impacted by the change in wavefield between source and receiver. Such changes are typically proportional to source-receiver distance on the order of the scales in this study (Green & Nippress, 2019). In the presence of realistic atmospheric multipathing, observing interstation similarity on the order of the 8 March 2017 Bogoslof eruption (Figure 2) across 2,000+ km is unlikely, particularly for weak signals. Short signals can be incorporated into a single envelope, and thus easily stacked (e.g., Hedlin & Walker, 2013). However, for signals

longer than a few minutes and for sources outside the network, stacking is more challenging and thus the true locations become difficult to resolve (Figure 11). In such cases, phase association and variable window lengths may be advantageous (Park et al., 2018), as well as allowing for multiple celerities at each time step between grid nodes and stations.

Seasonal variability in dominant stratospheric wind direction affects detection capability (Hedlin & Walker, 2013; Le Pichon et al., 2008; Le Pichon et al., 2009; Mutschlecner & Whitaker, 2010; Tailpied et al., 2017). In the Alaskan winter months, stratospheric winds typically blow eastward (from west to east) from the Aleutians toward the network, whereas in the summer the case is the opposite (De Angelis et al., 2012). In both cases, however, tropospheric and thermospheric ducting may still take place under different influences (De Angelis et al., 2012; de Groot-Hedlin, 2017; Iezzi et al., 2019; Schwaiger et al., 2019, 2020). Surface winds can also mask signals of interest, though such winds are typically weaker inland. Increased snow cover during winter can be beneficial by isolating sensors from turbulence and gusts (Woodward et al., 2005). It is reasonable that different parameter choices would work better at some times of year than others, for different event characteristics, and for different station combinations (Figure 10). For example, the lower frequency filter limit of 0.35 Hz is set in order to retain data above the microbarom peak and reduce wind noise. However, given the seasonal change in strength of the microbarom in the northern Pacific (Garcés et al., 2010; Walker, 2012), such a lower limit could be made flexible to take advantage of this situation.

The factors discussed above are interpreted here to affect the ROC classification, event-detection rates, and location accuracy results presented in section 3.4. The temporal features observed in Figure 10 are also reflected in results from other AGC and stacking methods (section S4, supporting information). However, the number of events in any particular month and their relative or absolute amplitudes are also important considerations when interpreting temporal statistics (including Figures 5 and 8). Given that ROC classification is performed with only Bogoslof events, rather than all known volcanic or nonvolcanic infrasound-generating signals, a more detailed assessment may produce improved results. In a similar vein, it is worth noting that the final AVO catalog was a retroactive assessment of data products, with some infrasound detections based on just a single array.

The choice of the DF type also affects the capacity for isolating, detecting, and locating explosive events, depending on the station configuration and event duration. Synthetic results show clear differences between DF types for the 1-min events (Figure 11a), and would be expected for sources up to several minutes. For Bogoslof, AVO cataloged infrasound durations vary from 2–409 min (median 14 min), with 17 of the 61 events $\leq$5 min. For out-of-network sources, STW-DFs have relatively clear peaks compared to TS-DFs (Figure 11a). This factor may contribute to the relatively high event detection rates for the single-sensor stations using STW-DFs (Figure 10). These implications extend to Cleveland, which is more remote than Bogoslof, and typically exhibits brief explosive eruptions (De Angelis et al., 2012; Werner et al., 2017; Iezzi et al., 2019; Table S2). However, Figure 10 shows that for combined and array station configurations, TS-DFs have a slight advantage for both reducing false positives, and for location accuracy of detected events.

Overall, 72% and 85% of known infrasound-generating events from Bogoslof were identified with TS-DF and STW-DF methodologies respectively, when using all sensors. Successful detections include the onset of the Bogoslof eruption sequence on 12 December 2016, and the following three events (section S2, supporting information), something not observed at the time by routine AVO monitoring (Coombs et al., 2018). Had Bogoslof been suspected of unrest, however, alarms at AVO arrays would likely have been set and triggered by the eruptions (Lyons et al., 2020). Detection of these events with RTM is in addition to several other cataloged events not documented as having detectable infrasound by AVO (section 3.1). Larger explosive events, such as the 2008 eruptions of Kasatochi and Okmok volcanoes, Alaska (Fee, Steffke, & Garcés, 2010), would likely be detected and located well with the RTM algorithm, even in the presence of unfavorable acoustic propagation or other conditions. Supplementing the network with strategically placed sensors in quiet locations would also likely improve RTM performance (e.g., Biasi & Alvarez, 2018; Tailpied et al., 2017), as would refined wind noise suppression for TA sensors. Improved algorithm performance is expected in areas with less challenging network geometries and weather conditions.

5. Conclusions

We have shown that simple RTM methods using the TA and other regional network infrasound data are capable of detecting and locating relatively small and emergent events from remote Alaskan volcanoes such as Bogoslof and Cleveland. Our RTM implementation is able to detect and locate more than 72% of the Bogoslof infrasound events cataloged by AVO. Such statistics, as well as those for location accuracy and classification success, vary significantly with RTM parameters choices. Identification and location of events with RTM is improved by the presence of the TA; however, individually, the TA typically performs worse than existing infrasound arrays in the region. This deficit is likely due to a combined function of greater source-station distances, lower azimuthal coverage, and lower intersensor signal coherence. Our efforts to locate infrasound signals from known eruptions in Kamchatka had a low success rate (one of five) due to more extreme cases of the above factors. The presence of spatial wind noise filters at most arrays is also a key difference versus TA sites. The effectiveness of RTM in the region also varies seasonally, with no apparent dependence on event size. Lower event detection rates during the summer, when stratospheric winds typically blow away from the network, show that increased azimuthal coverage of remote volcanoes is crucial and not compensated for by high sensor quantity alone. Opportunities for refining and improving these RTM strategies include data-adaptive processing, provision for atmospheric specifications, and incorporating azimuthal information from arrays. The frequent eruptions and dense regional network in Alaska provide an excellent opportunity to continue assessing the capability of regional-scale seismoacoustic networks for remote volcanic monitoring.

Acknowledgments

We acknowledge and thank the Alaska Volcano Observatory for collecting and supplying detailed volcanic event information, as well as operators of the monitoring networks and data management centers this study benefited directly from. For the study period, we downloaded TA, AEC, IMS, and GSN data from the IRIS DMC (https://www.iris.edu/, network codes TA, AK, IM, and II); AVO station data were obtained from the USGS Winston Wave Server (http://pubavo1.wr.usgs.gov:16023/menu, network code AV). We thank David Green, Aaron Wech, Michelle Coombs, and two anonymous reviewers for their comments that helped to improve the manuscript. We thank Curt Szuberla, Toshiro Tanimoto, Chen Ji, Zach Eilon, and Schemes Erickson for helpful discussions. We also thank IT staff at the Earth Research Institute (UC Santa Barbara) and acknowledge use of their high-performance computing systems. We also acknowledge the many software packages used for data processing and plotting, details being provided in section S5 of the supporting information. Data from the TA network were made freely available as part of the EarthScope USArray facility, operated by Incorporated Research Institutions for Seismology (IRIS) and supported by the National Science Foundation, under Cooperative Agreement EAR-1261681. Global Seismographic Network (GSN) is a cooperative scientific facility operated jointly by the Incorporated Research Institutions for Seismology (IRIS), the United States Geological Survey (USGS), and the National Science Foundation (NSF), under Cooperative Agreement EAR-1261681. The facilities of IRIS Data Services, and specifically the IRIS Data Management Center, were used for access to waveforms, related metadata, and/or derived products used in this study. IRIS Data Services are funded through the Seismological Facilities for the Advancement of Geoscience and EarthScope (SAGE) Proposal of the National Science Foundation under Cooperative Agreement EAR-1261681. Use was made of computational facilities purchased with funds from the National Science Foundation (CNS-1725797) and administered by the Center for Scientific Computing (CSC). The CSC is supported by the California NanoSystems Institute and the Materials Research Science and Engineering Center (MRSEC; NSF DMR 1720256) at UC Santa Barbara. This work was funded by NSF grants EAR-1614855 and EAR-1614323.

References

Alaska Volcano Observatory (2019). Volcano information: Eruption search. Retrieved from https://www.avo.alaska.edu/volcanoes/eruptsearch.php

Arrowsmith, S., Young, C., & Pankow, K. (2018). Implementation of the Waveform Correlation Event Detection System (WCEDS) method for regional seismic event detection in Utah. *Bulletin of the Seismological Society of America*, *108*(6), 3548–3356. https://doi.org/10.1785/0120180097

Batubara, M., Saito, H., & Yamamoto, M. Y. (2018). *Results from infrasound monitoring using integrated sensors data by means of a network along multisite point over Japan*. Abstract [S53D-0438] presented at 2018 Fall Meeting, AGU, Washington, DC.

Behnke, S. A., & McNutt, S. R. (2014). Using lightning observations as a volcanic eruption monitoring tool. *Bulletin of Volcanology*, *76*(8), 1–12. https://doi.org/10.1007/s00445-014-0847-1

Biasi, G. P., & Alvarez, M. G. (2018). Station and telemetry impact metrics for earthquake early warning seismic network performance evaluation (abstract). *Seismological Research Letters*, *89*(2B), 717–996.

Blackburn, L. (2015). Point and focus algorithms. Retrieved from https://eht-wiki.haystack.mit.edu/Public_Area/LMT/Point_and_focus_algorithms

Busby, R. W., Woodward, R. L., Hafner, K. A., Vernon, F. L., & Frassetto, A. M. (2018). The design and implementation of EarthScope's USArray Transportable Array in the Conterminous United States and Southern Canada. Retrieved from: http://www.usarray.org/researchers/obs/transportable/l48_ta_report

Cameron, C. E., Schaefer, J. R., & Mulliken, K. M. (2018). Historically active volcanoes of Alaska (Alaska Division of Geological & Geophysical Surveys Miscellaneous Publication 133 v. 3, 2 sheets). http://doi.org/10.14509/30142

Chouet, B. A., & Matoza, R. S. (2013). A multi-decadal view of seismic methods for detecting precursors of magma movement and eruption. *Journal of Volcanology and Geothermal Research*, *252*, 108–175. https://doi.org/10.1016/j.jvolgeores.2012.11.013

Cochran, E., & Shearer, P. (2006). Infrasound events detected with the Southern California Seismic Network. *Geophysical Research Letters*, *33*, L19803. https://doi.org/10.1029/2006GL026951

Coombs, M. L., Wallace, K., Cameron, C., Lyons, J. J., Wech, A., Angeli, K., & Cervelli, P. (2019). Overview, chronology, and impacts of the 2016–2017 eruption of Bogoslof volcano, Alaska. *Bulletin of Volcanology*, *81*(11), 1–23. https://doi.org/10.1007/s00445-019-1322-9

Coombs, M. L., Wech, A. G., Haney, M. M., Lyons, J. J., Schneider, D. J., Schwaiger, H. F., et al. (2018). Short-term forecasting and detection of explosions during the 2016–2017 eruption of Bogoslof volcano, Alaska. *Frontiers of Earth Science*, *6*(122). https://doi.org/10.3389/feart.2018.00122

Dabrowa, A. L., Green, D. N., Rust, A. C., & Phillips, J. C. (2011). A global study of volcanic infrasound characteristics and the potential for long-range monitoring. *Earth and Planetary Science Letters*, *310*(3–4), 369–379. https://doi.org/10.1016/j.epsl.2011.08.027

De Angelis, S., Fee, D., Haney, M., & Schneider, D. (2012). Detecting hidden volcanic explosions from Mt. Cleveland Volcano, Alaska with infrasound and ground-coupled airwaves. *Geophysical Research Letters*, *39*, L21312. https://doi.org/10.1029/2012GL053635

de Groot-Hedlin, C. D. (2017). Infrasound propagation in tropospheric ducts and acoustic shadow zones. *The Journal of the Acoustical Society of America*, *142*(4), 1816–1827. https://doi.org/10.1121/1.5005889

de Groot-Hedlin, C. D., & Hedlin, M. A. H. (2015). A method for detecting and locating geophysical events using groups of arrays. *Geophysical Journal International*, *203*(2), 960–971. https://doi.org/10.1093/gji/ggv345

de Groot-Hedlin, C. D., & Hedlin, M. A. H. (2018). A new automated approach to detecting and locating seismic events using data from a large network. *Bulletin of the Seismological Society of America*, *108*(4), 2032–2045. https://doi.org/10.1785/0120180072

de Groot-Hedlin, C. D., Hedlin, M. A. H., & Walker, K. T. (2014). Detection of gravity waves across the USArray: A case study. *Earth and Planetary Science Letters*, *402*, 346–352. https://doi.org/10.1016/j.epsl.2013.06.042

de Groot-Hedlin, C. D., Hedlin, M. A. H., Walker, K. T., Drob, D. P., & Zumberge, M. A. (2008). Evaluation of infrasound signals from the shuttle Atlantis using a large seismic network. *The Journal of the Acoustical Society of America*, *124*(3), 1442–1451. https://doi.org/10.1121/1.2956475

Drob, D. P., Picone, J. M., & Garcés, M. (2003). Global morphology of infrasound propagation. *Journal of Geophysical Research: Atmospheres*, *108*, D21. https://doi.org/10.1029/2002JD003307

Edwards, W. N., de Groot-Hedlin, C. D., & Hedlin, M. A. H. (2014). Forensic investigation of a probable meteor sighting using USArray acoustic data. *Seismological Research Letters*, *85*(5), 1012–1018. https://doi.org/10.1785/0220140056

Evers, L. G., & Haak, H. W. (2005). The detectability of infrasound in the Netherlands from the Italian volcano Mt. Etna. *Journal of Atmospheric and Solar: Terrestrial Physics*, *67*(3), 259–268. https://doi.org/10.1016/j.jastp.2004.09.002

Fan, W., de Groot-Hedlin, C. D., Hedlin, M. A. H., & Ma, Z. (2018). Using surface waves recorded by a large mesh of three-element arrays to detect and locate disparate seismic sources. *Geophysical Journal International*, *215*(2), 942–958. https://doi.org/10.1093/gji/ggy316

Fawcett, T. (2006). An introduction to ROC analysis. *Pattern Recognition Letters*, *27*, 861–874. https://doi.org/10.1016/j.patrec.2005.10.010

Fee, D., Garcés, M., Patrick, M., Chouet, B., Dawson, P., & Swanson, D. (2010). Infrasonic harmonic tremor and degassing bursts from Halema'uma'u Crater, Kilauea Volcano, Hawaii. *Journal of Geophysical Research: Solid Earth*, *115*, B11316. https://doi.org/10.1029/2010JB007642

Fee, D., Haney, M., Matoza, R., Szuberla, C., Lyons, J., & Waythomas, C. (2016). Seismic envelope-based detection and location of ground-coupled airwaves from volcanoes in Alaska. *Bulletin of the Seismological Society of America*, *106*(3), 1–12. https://doi.org/10.1785/0120150244

Fee, D., Haney, M. M., Matoza, R. S., Van Eaton, A. R., Cervelli, P., Schneider, D. J., & Iezzi, A. M. (2017). Volcanic tremor and plume height hysteresis from Pavlof Volcano, Alaska. *Science*, *355*(6320), 45–48. https://doi.org/10.1126/science.aah6108

Fee, D., Lyons, J., Haney, M., Wech, A., Waythomas, C. F., Diefenbach, A. K., et al. (2020). Seismo-acoustic evidence for vent drying during shallow submarine eruptions at Bogoslof volcano, Alaska. *Bulletin of Volcanology*, *82*(1), 1–14. https://doi.org/10.1007/s00445-019-1326-5

Fee, D., & Matoza, R. S. (2013). An overview of volcano infrasound: From Hawaiian to Plinian, local to global. *Journal of Volcanology and Geothermal Research*, *249*, 123–139. https://doi.org/10.1016/j.jvolgeores.2012.09.002

Fee, D., McNutt, S. R., Lopez, T. M., Arnoult, K. M., Szuberla, C. A. L., & Olson, J. V. (2013). Combining local and remote infrasound recordings from the 2009 Redoubt Volcano eruption. *Journal of Volcanology and Geothermal Research*, *259*, 100–114. https://doi.org/10.1016/j.jvolgeores.2011.09.012

Fee, D., Steffke, A., & Garcés, M. (2010). Characterization of the 2008 Kasatochi and Okmok eruptions using remote infrasound arrays. *Journal of Geophysical Research: Atmospheres*, *115*, D00L10. https://doi.org/10.1029/2009JD013621

Garcés, M., Fee, D., Steffke, A., McCormack, D., Servranckx, R., Bass, H., et al. (2008). Capturing the acoustic fingerprint of stratospheric ash injection. *EOS Transactions AGU*, *89*(40), 377–380. https://doi.org/10.1029/2008EO400001

Garcés, M., Willis, M., & Le Pichon, A. (2010). Infrasonic observations of open ocean swells in the Pacific: Deciphering the song of the sea. In A. Le Pichon, E. Blanc, & A. Hauchecorne (Eds.), *Infrasound monitoring for atmospheric studies*, (pp. 235–248). Dordrecht: Springer. https://doi.org/10.1007/978-1-4020-9508-5_7

Gibbons, S., Kværna, T., & Näsholm, P. (2019). Characterization of the infrasonic wavefield from repeating seismo-acoustic events. In A. Le Pichon, E. Blanc, & A. Hauchecorne (Eds.), *Infrasound monitoring for atmospheric studies: Challenges in middle-atmosphere dynamics and societal benefits*, (pp. 387–407). Cham: Springer. https://doi.org/10.1007/978-3-319-75140-5_10

Gibbons, S. J., Kværna, T., & Ringdal, F. (2005). Monitoring of seismic events from a specific source region using a single regional array: A case study. *Journal of Seismology*, *9*(3), 277–294. https://doi.org/10.1007/s10950-005-5746-7

Godin, O. A. (2008). Sound transmission through water–air interfaces: New insights into an old problem. *Contemporary Physics*, *49*(2), 105–123. https://doi.org/10.1080/00107510802090415

Gordeev, E. I., Firstov, P. P., Kulichkov, S. N., & Makhmudov, E. R. (2013). *Izvestiya, Atmospheric and Oceanic Physics*, *49*(4), 420–431. https://doi.org/10.1134/S0001433813030080

Green, D. N., & Nippress, A. (2019). Infrasound signal duration: The effects of propagation distance and waveguide structure. *Geophysical Journal International*, *216*(3), 1974–1988. https://doi.org/10.1093/gji/ggy530

Haney, M. M. (2010). Location and mechanism of very long period tremor during the 2008 eruption of Okmok Volcano from interstation arrival times. *Journal of Geophysical Research: Solid Earth*, *115*, B00B05. https://doi.org/10.1029/2010JB007440

Haney, M. M., Fee, D., McKee, K. F., Lyons, J. J., Matoza, R. S., Wech, A. G., et al. (2020). Co-eruptive tremor from Bogoslof volcano: Seismic wavefield composition at regional distances. *Bulletin of Volcanology*, *82*(2), 1–14. https://doi.org/10.1007/s00445-019-1347-0

Haney, M. M., Van Eaton, A. R., Lyons, J. J., Kramer, R. L., Fee, D., Iezzi, A. M., et al. (2020). Characteristics of thunder and electromagnetic pulses from volcanic lightning at Bogoslof volcano, Alaska. *Bulletin of Volcanology*, *82*(2), 1–16. https://doi.org/10.1007/s00445-019-1349-y

Harris, A., & Ripepe, M. (2007). Synergy of multiple geophysical approaches to unravel explosive eruption conduit and source dynamics—A case study from Stromboli. *Geochemistry*, *67*(1), 1–35. https://doi.org/10.1016/j.chemer.2007.01.003

Havskov, J., & Alguacil, G. (2016). Seismic Arrays. In *Instrumentation in earthquake seismology*, (pp. 309–329). Cham: Springer. https://doi.org/10.1007/978-3-319-21314-9_9

Hedlin, M. A. H., & Walker, K. T. (2013). A study of infrasonic anisotropy and multipathing in the atmosphere using seismic networks. *Philosophical Transactions of the Royal Society A*, *371*, 20110542. https://doi.org/10.1098/rsta.2011.0542

Ichihara, M., Ripepe, M., Goto, A., Oshima, H., Aoyama, H., Iguchi, M., et al. (2009). Airwaves generated by an underwater explosion: Implications for volcanic infrasound. *Journal of Geophysical Research: Solid Earth*, *114*, B03210. https://doi.org/10.1029/2008JB005792

Iezzi, A. M., Schwaiger, H. F., Fee, D., & Haney, M. M. (2019). Application of an updated atmospheric model to explore volcano infrasound propagation and detection in Alaska. *Journal of Volcanology and Geothermal Research*, *371*, 192–205. https://doi.org/10.1016/j.jvolgeores.2018.03.009

IRIS DMC (2012). Data services products: Infrasound TA infrasound data products. https://doi.org/10.17611/DP/IS.1

IRIS DMC (2014). TA infrasound reference event database: Mudslide, OSO WA. Retrieved from http://ds.iris.edu/spud/infrasoundevent/12677316

Johnson, J. B., & Aster, R. C. (2005). Relative partitioning of acoustic and seismic energy during Strombolian eruptions. *Journal of Volcanology and Geothermal Research*, *148*(3–4), 334–354. https://doi.org/10.1016/j.jvolgeores.2005.05.002

Johnson, J. B., Aster, R. C., Ruiz, M. C., Malone, S. D., McChesney, P. J., Lees, J. M., & Kyle, P. R. (2003). Interpretation and utility of infrasonic records from erupting volcanoes. *Journal of Volcanology and Geothermal Research*, *121*(1–2), 15–63. https://doi.org/10.1016/S0377-0273(02)00409-2

Johnson, J. B., & Ripepe, M. (2011). Volcano infrasound: A review. *Journal of Volcanology and Geothermal Research*, *206*(3–4), 61–69. https://doi.org/10.1016/j.jvolgeores.2011.06.006

Jolly, A. D., Matoza, R. S., Fee, D., Kennedy, B. M., Iezzi, A. M., Fitzgerald, R. H., et al. (2017). Capturing the acoustic radiation pattern of Strombolian eruptions using infrasound sensors aboard a tethered aerostat, Yasur volcano, Vanuatu. *Geophysical Research Letters*, *44*, 9672–9680. https://doi.org/10.1002/2017GL074971

Jones, K. R., & Johnson, J. B. (2011). Mapping complex vent eruptive activity at Santiaguito, Guatemala using network infrasound semblance. *Journal of Volcanology and Geothermal Research*, *199*(1–2), 15–24. https://doi.org/10.1016/j.jvolgeores.2010.08.006

Jónsdóttir, K., Ripepe, M., Barsotti, S., Björnsson, H., Del Donne, D., & Vogfjörð, K. (2015). Infrasound network implementation in Iceland - examples of volcano monitoring in an extreme environment. *Geophysical Research Abstracts*, *17*, EGU2015-11869.

Kim, K., & Lees, J. M. (2015). Imaging volcanic infrasound sources using time reversal mirror algorithm. *Geophysical Journal International*, *202*(3), 1663–1676. https://doi.org/10.1093/gji/ggv237

Koper, K. D., Hutko, A. R., Lay, T., & Sufri, O. (2012). Imaging short-period seismic radiation from the 27 February 2010 Chile (M_W 8.8) earthquake by back-projection of *P*, *PP*, and *PKIKP* waves. *Journal of Geophysical Research: Solid Earth*, *117*, B02308. https://doi.org/10.1029/2011JB008576

KVERT, Institute of Volcanology and Seismology FEB RAS (2019). VONA/KVERT information releases. Retrieved from: http://www.kscnet.ru/ivs/kvert/van/index.php

Landès, M., Ceranna, L., Le Pichon, A., & Matoza, R. S. (2012). Localization of microbarom sources using the IMS infrasound network. *Journal of Geophysical Research: Atmospheres*, *117*, D06102. https://doi.org/10.1029/2011JD016684

Le Pichon, A., Blanc, E., Drob, D., Lambotte, S., Dessa, J. X., Lardy, M., et al. (2005). Infrasound monitoring of volcanoes to probe high-altitude winds. *Journal of Geophysical Research: Atmospheres*, *110*, D13106. https://doi.org/10.1029/2004JD005587

Le Pichon, A., Vergoz, J., Blanc, E., Guilbert, J., Ceranna, L., Evers, L., & Brachet, N. (2009). Assessing the performance of the International Monitoring System's infrasound network: Geographical coverage and temporal variabilities. *Journal of Geophysical Research: Atmospheres*, *114*, D08112. https://doi.org/10.1029/2008JD010907

Le Pichon, A., Vergoz, J., Herry, P., & Ceranna, L. (2008). Analyzing the detection capability of infrasound arrays in central Europe. *Journal of Geophysical Research: Atmospheres*, *113*, D12115. https://doi.org/10.1029/2007JD009509

Lees, J. M., Gordeev, E. I., & Ripepe, M. (2004). Explosions and periodic tremor at Karymsky Volcano, Kamchatka, Russia. *Geophysical Journal International*, *158*(3), 1151–1167. http://doi.org/10.1111/j.1365-246X.2004.02239.x

Liszka, L., & Garcés, M. A. (2002). Infrasonic observations of the Hekla eruption of February 26, 2000. *Journal of Low Frequency Noise, Vibration and Active Control*, *21*(1), 1–8. https://doi.org/10.1260/02630920260374934

Lopez, T., Clarisse, L., Schwaiger, H., Van Eaton, A., Loewen, M., Fee, D., et al. (2020). Constraints on eruption processes and event masses for the 2016–2017 eruption of Bogoslof volcano, Alaska, through evaluation of IASI satellite SO2 masses and complementary datasets. *Bulletin of Volcanology*, *82*(2), 1–17. https://doi.org/10.1007/s00445-019-1348-z

Lyons, J. J., Haney, M. M., Fee, D., Wech, A. G., & Waythomas, C. F. (2019). Infrasound from giant bubbles during explosive submarine eruptions of Bogoslof volcano, Alaska. *Nature Geoscience*, *12*(11), 952–958. https://doi.org/10.1038/s41561-019-0461-0

Lyons, J. J., Iezzi, A. M., Fee, D., Schwaiger, H. F., Wech, A. G., & Haney, M. M. (2020). Infrasound generated by the 2016–17 shallow submarine eruption of Bogoslof volcano, Alaska. *Bulletin of Volcanology*, *82*(19). https://doi.org/10.1007/s00445-019-1355-0

Marchetti, E., Ichihara, M., & Ripepe, M. (2004). Propagation of acoustic waves in a viscoelastic two-phase system: Influence of gas bubble concentration. *Journal of Volcanology and Geothermal Research*, *137*(1–3), 93–108. https://doi.org/10.1016/j.jvolgeores.2004.05.002

Marchetti, E., Ripepe, M., Delle Donne, D., Genco, R., Finizola, A., & Garaebiti, E. (2013). Blast waves from violent explosive activity at Yasur Volcano, Vanuatu. *Geophysical Research Letters*, *40*, 5838–5843. https://doi.org/10.1002/2013GL057900

Matoza, R. S., Fee, D., & Garcés, M. A. (2010). Infrasonic tremor wavefield of the Pu'u'Ō'ō crater complex and lava tube system, Hawaii, in April 2007. *Journal of Geophysical Research: Solid Earth*, *115*, B12312. https://doi.org/10.1029/2009JB007192

Matoza, R., Fee, D., Green, D., & Mialle, P. (2019). Volcano infrasound and the International Monitoring System. In A. Le Pichon, E. Blanc, & A. Hauchecorne (Eds.), *Infrasound monitoring for atmospheric studies: Challenges in middle-atmosphere dynamics and societal benefits*, (pp. 1023–1077). Cham: Springer. https://doi.org/10.1007/978-3-319-75140-5_33

Matoza, R. S., Fee, D., Green, D. N., Le Pichon, A., Vergoz, J., Haney, M. M., et al. (2018). Local, regional, and remote seismo-acoustic observations of the April 2015 VEI 4 eruption of Calbuco volcano, Chile. *Journal of Geophysical Research: Solid Earth*, *123*, 3814–3827. https://doi.org/10.1002/2017JB015182

Matoza, R. S., Green, D. N., Le Pichon, A., Shearer, P. M., Fee, D., Mialle, P., & Ceranna, L. (2017). Automated detection and cataloging of global explosive volcanism using the International Monitoring System infrasound network. *Journal of Geophysical Research: Solid Earth*, *122*, 2946–2971. https://doi.org/10.1002/2016JB013356

Matoza, R. S., Hedlin, M. A. H., & Garcés, M. A. (2007). An infrasound array study of Mount St. Helens. *Journal of Volcanology and Geothermal Research*, *160*(3–4), 249–262. https://doi.org/10.1016/j.jvolgeores.2006.10.006

Matoza, R. S., Landès, M., Le Pichon, A., Ceranna, L., & Brown, D. (2013). Coherent ambient infrasound recorded by the International Monitoring System. *Geophysical Research Letters*, *40*, 429–433. https://doi.org/10.1029/2012GL054329

Matoza, R. S., Le Pichon, A., Vergoz, J., Herry, P., Lalande, J.-M., Lee, H.-I., et al. (2011). Infrasonic observations of the June 2009 Sarychev Peak eruption, Kuril Islands: Implications for infrasonic monitoring of remote explosive volcanism. *Journal of Volcanology and Geothermal Research*, *200*, 35–48. https://doi.org/10.1016/j.jvolgeores.2010.11.022

Matoza, R. S., Vergoz, J., Le Pichon, A., Ceranna, L., Green, D. N., Evers, L. G., et al. (2011). Long-range acoustic observations of the Eyjafjallajökull eruption, Iceland, April–May 2010. *Geophysical Research Letters*, *38*, L06308. https://doi.org/10.1029/2011GL047019

McNutt, S. R., & Williams, E. R. (2010). Volcanic lightning: Global observations and constraints on source mechanisms. *Bulletin of Volcanology*, *72*(10), 1153–1167. https://doi.org/10.1007/s00445-010-0393-4

Meng, L., Ampuero, J. P., Luo, Y., Wu, W., & Ni, S. (2012). Mitigating artifacts in back-projection source imaging with implications for frequency-dependent properties of the Tohoku-Oki earthquake. *Earth, Planets and Space*, *64*(12), 1101–1109. https://doi.org/10.5047/eps.2012.05.010

Mialle, P., Brachet, N., Gaillard, P., Le Pichon, A., Blanc, E., Tailpied, D., et al. (2015). *Towards a volcanic notification system with infrasound data: Use of infrasound data in support of the VAACs in the framework of ARISE project*. Abstract [T1.1-O4] presented at 2015 Science and Technology Conference, Vienna, Austria.

Mikumo, T., & Watada, S. (2010). Acoustic-gravity waves from earthquake sources. In A. Le Pichon, E. Blanc, & A. Hauchecorne (Eds.), *Infrasound monitoring for atmospheric studies*, (pp. 263–279). Dordrecht: Springer. https://doi.org/10.1007/978-1-4020-9508-5_9

Mutschlecner, J. P., & Whitaker, R. W. (2010). Some atmospheric effects on infrasound signal amplitudes. In A. Le Pichon, E. Blanc, & A. Hauchecorne (Eds.), *Infrasound monitoring for atmospheric studies*, (pp. 455–474). Dordrecht: Springer. https://doi.org/10.1007/978-1-4020-9508-5_14

National Academies of Sciences, Engineering, & Medicine (2017). Volcanic eruptions and their repose, unrest, precursors, and timing. *Washington, DC: The National Academies Press.* https://doi.org/10.17226/24650

Park, J., Hayward, C., & Stump, B. W. (2018). Assessment of infrasound signals recorded on seismic stations and infrasound arrays in the western United States using ground truth sources. *Geophysical Journal International*, *213*(3), 1608–1628. https://doi.org/10.1093/gji/ggy042

Perttu, A., Taisne, B., Williams, R., & Tailpied, D. (2018). Quantifying detection capability of a regional infrasound network using a combination of film sound techniques and array processing. *Geophysical Research Abstracts*, *20*, EGU2018–EGU13229.

Petersen, T., De Angelis, S., Tytgat, G., & McNutt, S. R. (2006). Local infrasound observations of large ash explosions at Augustine Volcano, Alaska, during January 11–28, 2006. *Geophysical Research Letters*, *33*, L12303. https://doi.org/10.1029/2006GL026491

Petersen, T., & McNutt, S. R. (2007). Seismo-acoustic signals associated with degassing explosions recorded at Shishaldin Volcano, Alaska, 2003–2004. *Bulletin of Volcanology*, *69*(5), 527–536. https://doi.org/10.1007/s00445-006-0088-z

Pinsky, V., Blom, P., Polozov, A., Marcillo, O., Arrowsmith, S., & Hofstetter, A. (2017). Towards an accurate real-time locator of infrasonic sources. *Journal of Seismology*, *21*(6), 1361–1383. https://doi.org/10.1007/s10950-017-9670-4

Pyle, D. M., Mather, T. A., & Biggs, J. (Eds.). (2013). Remote sensing of volcanoes and volcanic processes: Integrating observation and modelling. *Geological Society, London, Special Publications*, *380*. https://doi.org/10.1144/SP380.0

Raspet, R., Abbott, J.-P., Webster, J., Yu, J., Talmadge, C., Alberts, K. II, et al. (2019). New systems for wind noise reduction for infrasonic measurements. In A. Le Pichon, E. Blanc, & A. Hauchecorne (Eds.), *Infrasound monitoring for atmospheric studies: Challenges in middle-atmosphere dynamics and societal benefits*, (pp. 91–124). Cham: Springer. https://doi.org/10.1007/978-3-319-75140-5_3

Ripepe, M., Marchetti, E., Delle Donne, D., Genco, R., Innocenti, L., Lacanna, G., & Valade, S. (2018). Infrasonic early warning system for explosive eruptions. *Journal of Geophysical Research: Solid Earth*, *123*, 9570–9585. https://doi.org/10.1029/2018JB015561

Ripepe, M., Marchetti, E., & Ulivieri, G. (2007). Infrasonic monitoring at Stromboli volcano during the 2003 effusive eruption: Insights on the explosive and degassing process of an open conduit system. *Journal of Geophysical Research*, *112*, B09207. https://doi.org/10.1029/2006JB004613

Ruiz, M., Lees, J., & Johnson, J. B. (2006). Source constraints of Tungurahua volcano explosion events. *Bulletin of Volcanology*, *68*(5), 480–490. https://doi.org/10.1007/s00445-005-0023-8

Schneider, F. M., Fuchs, F., Kolínský, P., Caffagni, E., Serafin, S., Dorninger, M., Bokelmann, G., & AlpArray Working Group (2018). Seismo-acoustic signals of the Baumgarten (Austria) gas explosion detected by the AlpArray seismic network. *Earth and Planetary Science Letters*, *502*, 104–114. https://doi.org/10.1016/j.epsl.2018.08.034

Schwaiger, H. F., Iezzi, A. M., & Fee, D. (2019). AVO-G2S: A modified, open-source Ground-to-Space atmospheric specification for infrasound modeling. *Computers & Geosciences*, *125*, 90–97. https://doi.org/10.1016/j.cageo.2018.12.013

Schwaiger, H. F., Lyons, J. J., Iezzi, A. M., Fee, D., & Haney, M. M. (2020). Evolving infrasound detections from Bogoslof volcano, Alaska: Insights from atmospheric propagation modeling. *Bulletin of Volcanology*. https://doi.org/10.1007/s00445-020-1360-3

Searcy, C. K., & Power, J. A. (2020). Seismic character and progression of explosive activity during the 2016–2017 eruption of Bogoslof volcano, Alaska. *Bulletin of Volcanology*, *82*(1), 1–15. https://doi.org/10.1007/s00445-019-1343-4

Shang, C., Teng, P., Lyu, J., Yang, J., & Sun, H. (2019). Infrasonic source altitude localization based on an infrasound ray tracing propagation model. *The Journal of the Acoustical Society of America*, *145*(6), 3805–3816. https://doi.org/10.1121/1.5110712

Shani-Kadmiel, S., Assink, J., Fee, D., & Evers, L. (2018). Special event: North of Anchorage, Alaska: International Monitoring System (IMS) array IM.I53US. Retrieved from http://ds.iris.edu/ds/nodes/dmc/specialevents/2018/11/30/north-of-anchorage-alaska/

Shani-Kadmiel, S., Assink, J. D., Smets, P. S. M., & Evers, L. G. (2018). Seismoacoustic coupled signals from earthquakes in central Italy: Epicentral and secondary sources of infrasound. *Geophysical Research Letters*, *45*. https://doi.org/10.1002/2017GL076125

Shearer, P. (1994). Global seismic event detection using a matched filter on long-period seismograms. *Journal of Geophysical Research: Solid Earth*, *99*, B7. https://doi.org/10.1029/94JB00498

Szuberla, C. A. L., Arnoult, K. M., & Olson, J. V. (2006). Discrimination of near-field infrasound sources based on time-difference of arrival information. *The Journal of the Acoustical Society of America*, *120*(3), EL23–EL28. https://doi.org/10.1121/1.2234517

Szuberla, C. A. L., & Olson, J. V. (2004). Uncertainties associated with parameter estimation in atmospheric infrasound arrays. *The Journal of the Acoustical Society of America*, *115*(1), 253–258. https://doi.org/10.1121/1.1635407

Tailpied, D., Le Pichon, A., Marchetti, E., Assink, J., & Vergniolle, S. (2017). Assessing and optimizing the performance of infrasound networks to monitor volcanic eruptions. *Geophysical Journal International*, *208*(1), 437–448. https://doi.org/10.1093/gji/ggw400

Tepp, G., Dziak, R. P., Haney, M. M., Lyons, J. J., Searcy, C., Matsumoto, H., & Haxel, J. (2020). Seismic and hydroacoustic observations of the 2016–17 Bogoslof eruption. *Bulletin of Volcanology*, *82*(1), 1–21. https://doi.org/10.1007/s00445-019-1344-3

Tepp, G., & Haney, M. M. (2019). Comparison of short-term seismic precursors and explosion parameters during the 2016–2017 Bogoslof eruption. *Bulletin of Volcanology*, *81*(11), 1–15. https://doi.org/10.1007/s00445-019-1323-8

Toney, L. D., Fee., D., Allstadt, K., Haney, M. M., & Matoza, R. S. (2019). *A tale of two very large avalanches: Probing the limits of seismoacoustic avalanche characterization on Iliamna Volcano, Alaska*. Abstract [S23D-0658] presented at 2019 Fall Meeting, AGU, San Francisco, CA.

USArray (2019). Transportable Array deployment to Alaska and Western Canada. Retrieved from http://www.usarray.org/alaska#station-design

Van Eaton, A. R., Amigo, À., Bertin, D., Mastin, L. G., Giacosa, R. E., González, J., et al. (2016). Volcanic lightning and plume dynamics reveal evolving hazards during the April 2015 eruption of Calbuco volcano, Chile. *Geophysical Research Letters*, *43*, 3563–3571. https://doi.org/10.1002/2016GL068076

Vergniolle, S., & Caplan-Auerbach, J. (2006). Basaltic thermals and Subplinian plumes: Constraints from acoustic measurements at Shishaldin volcano, Alaska. *Bulletin of Volcanology*, *68*(7–8), 611–630. https://doi.org/10.1007/s00445-005-0035-4

Walker, K. T. (2012). Evaluating the opposing wave interaction hypothesis for the generation of microbaroms in the eastern North Pacific. *Journal of Geophysical Research: Oceans*, *117*, C12016. https://doi.org/10.1029/2012JC008409

Walker, K. T., & Hedlin, M. A. (2010). A review of wind-noise reduction methodologies. In A. Le Pichon, E. Blanc, & A. Hauchecorne (Eds.), *Infrasound monitoring for atmospheric studies*, (pp. 141–182). Dordrecht: Springer. https://doi.org/10.1007/978-1-4020-9508-5_5

Walker, K. T., Hedlin, M. A. H., de Groot-Hedlin, C., Vergoz, J., Le Pichon, A., & Drob, D. P. (2010). Source location of the 19 February 2008 Oregon bolide using seismic networks and infrasound arrays. *Journal of Geophysical Research: Solid Earth*, *115*, B12. https://doi.org/10.1029/2010JB007863

Walker, K. T., Shelby, R., Hedlin, M. A., Groot-Hedlin, C., & Vernon, F. (2011). Western US infrasonic catalog: Illuminating infrasonic hot spots with the USArray. *Journal of Geophysical Research: Solid Earth*, *116*, B12. https://doi.org/10.1029/2011JB008579

Waxler, R. M. (2017). Infrasound phenomenology, propagation, and detection. *The Journal of the Acoustical Society of America*, *142*(4), 2529–2529. https://doi.org/10.1121/1.5014242

Waythomas, C. F., & Cameron, C. E. (2018). Historical eruptions and hazards at Bogoslof volcano, Alaska (U.S. Geological Survey scientific investigations report 2018–5085). https://doi.org/10.3133/sir20185085

Waythomas, C. F., Loewen, M., Wallace, K. L., Cameron, C. E., & Larsen, J. F. (2020). Geology and eruptive history of Bogoslof volcano. *Bulletin of Volcanology*, *82*(2), 1–23. https://doi.org/10.1007/s00445-019-1352-3

Waythomas, C. F., Scott, W. E., Prejean, S. G., Schneider, D. J., Izbekov, P., & Nye, C. J. (2010). The 7–8 August 2008 eruption of Kasatochi Volcano, central Aleutian Islands, Alaska. *Journal of Geophysical Research: Solid Earth*, *115*, B00B06. https://doi.org/10.1029/2010JB007437

Webley, P., & Mastin, L. (2009). Improved prediction and tracking of volcanic ash clouds. *Journal of Volcanology and Geothermal Research*, *186*(1–2), 1–9. https://doi.org/10.1016/j.jvolgeores.2008.10.022

Wech, A., Tepp, G., Lyons, J., & Haney, M. (2018). Using earthquakes, *T* waves, and infrasound to investigate the eruption of Bogoslof volcano, Alaska. *Geophysical Research Letters*, *45*(14), 6918–6925. https://doi.org/10.1029/2018GL078457

Werner, C., Kern, C., Coppola, D., Lyons, J. J., Kelly, P. J., Wallace, K. L., et al. (2017). Magmatic degassing, lava dome extrusion, and explosions from Mount Cleveland volcano, Alaska, 2011–2015: Insight into the continuous nature of volcanic activity over multi-year timescales. *Journal of Volcanology and Geothermal Research*, *337*, 98–110. https://doi.org/10.1016/j.jvolgeores.2017.03.001

Woodward, R., Israelsson, H., Bondár, I., McLaughlin, K., Bowman, J. R., & Bass, H. (2005). Understanding wind-generated infrasound noise. *Proceedings of the 27th Seismic Research Review: Ground-based nuclear explosion monitoring technologies*, 866–875. Retrieved from https://www.osti.gov/servlets/purl/1027447

Xu, Y., Koper, K. D., Sufri, O., Zhu, L., & Hutko, A. R. (2009). Rupture imaging of the M_w 7.9 12 May 2008 Wenchuan earthquake from back projection of teleseismic *P* waves. *Geochemistry, Geophysics, Geosystems*, *10*, Q04006. https://doi.org/10.1029/2008GC002335

References From the Supporting Information

Arnoult, K. M., Olson, J. V., Szuberla, C. A. L., McNutt, S. R., Garcés, M. A., Fee, D., & Hedlin, M. A. H. (2010). Infrasound observations of the 2008 explosive eruptions of Okmok and Kasatochi volcanoes, Alaska. *Journal of Geophysical Research: Atmospheres*, *115*, D00L15. https://doi.org/10.1029/2010jd013987

Bowman, J. R. (2005). Meteorological conditions at infrasound stations. *Inframatics*, *9*.

Bueno, A., Diaz-Moreno, A., Álvarez, I., De la Torre, A., Lamb, O. D., Zuccarello, L., & De Angelis, S. (2019). VINEDA – Volcanic INfrasound Explosions Detector Algorithm. *Frontiers in Earth Science*, *7*(335). https://doi.org/10.3389/feart.2019.00335

Carniel, R., Cabras, G., Ichihara, M., & Takeo, M. (2014). Filtering wind in infrasound data by non-negative matrix factorization. *Seismological Research Letters*, *85*(5), 1056–1062. https://doi.org/10.1785/0220130142

Fee, D., & Garcés, M. (2007). Infrasonic tremor in the diffraction zone. *Geophysical Research Letters*, *34*, L16826. https://doi.org/10.1029/2007GL030616

Green, D. N., Matoza, R. S., Vergoz, J., & Le Pichon, A. (2012). Infrasonic propagation from the 2010 Eyjafjallajökull eruption: Investigating the influence of stratospheric solar tides. *Journal of Geophysical Research: Atmospheres*, *117*, D21202. https://doi.org/10.1029/2012JD017988

Ham, F. M., Iyengar, I., Hambebo, B. M., Garcés, M., Deaton, J., Perttu, A., & Williams, B. (2012). A neurocomputing approach for monitoring Plinian volcanic eruptions using infrasound. *Procedia Computer Science*, *13*, 7–17. https://doi.org/10.1016/j.procs.2012.09.109

Olson, J. V. (1982). Noise suppression using data-adaptive polarization filters: Applications to infrasonic array data. *The Journal of the Acoustical Society of America*, *72*(5), 1456–1460. https://doi.org/10.1121/1.388679

Runco, A. M. Jr., Louthain, J. A., & Clauter, D. A. (2014). Optimizing the PMCC algorithm for infrasound and seismic nuclear treaty monitoring. *Open Journal of Acoustics*, *4*, 204–213. https://doi.org/10.4236/oja.2014.44020

Sit, S., Brudzinski, M., & Kao, H. (2012). Detecting tectonic tremor through frequency scanning at a single station: Application to the Cascadia margin. *Earth and Planetary Science Letters*, *353–354*, 134–144. https://doi.org/10.1016/j.epsl.2012.08.002

Tepp, G. (2018). A repeating event sequence alarm for monitoring volcanoes. *Seismological Research Letters*, *89*(5), 1863–1876. https://doi.org/10.1785/0220170263

Zhu, W., Mousavi, S. M., & Beroza, G. C. (2019). Seismic signal denoising and decomposition using deep neural networks. *IEEE Transactions on Geoscience and Remote Sensing*, *57*(11), 9476–9488. https://doi.org/10.1109/TGRS.2019.2926772